

Signatures of spin-glass superconductivity in nickelate (La, Pr, Sm)₃Ni₂O₇ films

Haoran Ji^{1#}, Zheyuan Xie^{1#}, Yaqi Chen^{2#}, Guangdi Zhou^{2,3#}, Longxin Pan^{4,5}, Heng Wang^{2,3}, Haoliang Huang^{2,3}, Jun Ge¹, Yi Liu^{4,5}, Guang-Ming Zhang⁶, Ziqiang Wang^{7*}, Qi-Kun Xue^{2,3,8}, Zhuoyu Chen^{2,3*} & Jian Wang^{1,9,10*}

¹International Center for Quantum Materials, School of Physics, Peking University, Beijing 100871, China

²State Key Laboratory of Quantum Functional Materials, Department of Physics, and Guangdong Basic Research Center of Excellence for Quantum Science, Southern University of Science and Technology, Shenzhen 518055, China

³Quantum Science Center of Guangdong-Hong Kong-Macao Greater Bay Area, Shenzhen, 518045, China

⁴Department of Physics and Beijing Key Laboratory of Opto-electronic Functional Materials & Micro-nano Devices, Renmin University of China, Beijing 100872, China

⁵Key Laboratory of Quantum State Construction and Manipulation (Ministry of Education), Renmin University of China, Beijing 100872, China

⁶School of Physical Science and Technology, ShanghaiTech University, Shanghai 201210, China

⁷ Department of Physics, Boston College, Chestnut Hill, MA 0246, USA

⁸ Department of Physics, Tsinghua University, Beijing, 100084, China

⁹ Collaborative Innovation Center of Quantum Matter, Beijing 100871, China

¹⁰ Hefei National Laboratory, Hefei 230088, China

[#]These authors contribute equally.

*Correspondence to: jianwangphysics@pku.edu.cn (J.W.),
chenzhuoyu@sustech.edu.cn (Z.C.),
wangzi@bc.edu (Z.W.)

The discovery of Ruddlesden-Popper (R-P) nickelate superconductors under high pressure heralds a new chapter of high-transition temperature (high- T_c) superconductivity¹⁻⁴. Recently, ambient-pressure superconductivity is achieved in R-P bilayer nickelate thin films through epitaxial compressive strain^{5,6}, unlocking in-depth investigations into the superconducting characteristics. Here, through electrical transport study, we report the observation of spin-glass superconductivity with hysteretic magnetoresistance and glass-like dynamics in the bilayer nickelate (La, Pr, Sm)₃Ni₂O₇ films. The superconductivity develops in a two-step transition, with onset T_c exceeding 50 K and zero-resistance T_c around 15 K. Remarkably, magnetoresistance hysteresis, indicative of time-reversal symmetry breaking, is observed exclusively during the second-step transition to zero resistance. The hysteresis is observed under both out-of-plane and in-plane magnetic fields with significant anisotropy, and exhibits coalescing minima at zero field, fundamentally distinct from trapped vortices or long-range-ordered magnetism with coercivity. Successive oxygen reductions simultaneously suppress the superconductivity and hysteresis, revealing their mutual connections to the selective electronic orbitals. The removal of magnetic field triggers spontaneous and logarithmically slow resistance relaxations in the second-step transition, signatures of glassy dynamics, indicating that the superconducting ground state is correlated with an electronic spin-glass order. Our findings uncover an unprecedented superconducting state in the nickelate superconductors, providing phenomenological and conceptual advances for future investigations on high- T_c superconductivity.

Since the discovery of high-transition temperature (high- T_c) superconductivity in the cuprates^{7,8}, layered oxides that are structural and electronic analogous to cuprates have been pursued for decades as potential candidates for high- T_c superconductivity⁹. Extending this strategy, superconductivity with T_c around 15 K was achieved in the infinite-layer nickelate $R_{1-x}\text{Sr}_x\text{NiO}_2$ ($R = \text{La, Pr, Nd, ...}$) thin films¹⁰, which share $3d^9$ electronic configuration (Ni^+) and are isostructural to the cuprates. Subsequently, in the Ruddlesden-Popper (R-P) nickelates $R_{n+1}\text{Ni}_n\text{O}_{3n+1}$ ($n = 1, 2, 3, \dots, \infty$), superconductivity with onset T_c near 80 K was discovered in bilayer (La, Pr)₃Ni₂O₇ and near 30 K in trilayer La₄Ni₃O₁₀ bulk crystals under high pressure^{1,3,4}, establishing the nickelate as a new family of high- T_c superconductors. Structurally, the R-P bilayer nickelates host the covalently bonded apical oxygen, which couples the adjacent Ni-O layer, and stabilizes a mixed-valence state of $\text{Ni}^{2.5+}$ with $3d^{7.5}$ configuration. The bilayer nickelates involve both $3d_{z^2}$ and $3d_{x^2-y^2}$ orbitals near the Fermi level^{1,11-17} and necessitate the consideration of interlayer coupling¹⁸⁻²¹, differing from the single-orbital picture of cuprates. In this regard, the bilayer nickelate superconductors with distinct electronic structures and strong electronic correlations immediately sparked extensive and

intensive research interests. Very recently, the discovery of superconductivity in (La, Pr)₃Ni₂O₇ thin films at ambient pressure via epitaxial compressive strain^{5,6,22} enables direct characterization of the bilayer nickelates through more available experimental techniques²³⁻²⁸, and opens the door for exceptional opportunities to understand the novel unconventional superconducting state.

Here, through systematic electrical transport measurements, we report the observation of an unconventional two-dimensional (2D) superconducting state with hysteretic magnetoresistance and glassy dynamics in bilayer nickelate (La, Pr, Sm)₃Ni₂O₇ films. With isovalent substitution of Pr and Sm, the La_{2.46}Pr_{0.24}Sm_{0.3}Ni₂O₇ film exhibits onset T_c exceeding 50 K and reaches zero-resistance state around 15 K, while the La_{2.85}Pr_{0.15}Ni₂O₇ film exhibits onset T_c around 45 K and zero-resistance state around 8 K. Both films show a remarkable two-step superconducting transition. Exclusively during the second-step transition that evolves into zero-resistance state, the evident magnetoresistance hysteresis is observed. The history-dependent hysteresis is irreversible under time-reversal operation, providing the direct evidence for spontaneous time-reversal symmetry (TRS) breaking. The hysteresis is observed under both out-of-plane and in-plane magnetic fields with significant anisotropy, and shows coalescing minima at zero field, rather than two split minima corresponding to coercivity. These distinctive properties preclude the mechanisms such as trapped vortices, remanent field, or long-range magnetic order. Moreover, the hysteresis is progressively suppressed with the reduced oxygen content that simultaneously weakens the superconductivity, suggesting its underlying connection to selective Ni-3d electronic orbitals. Crucially, after the removal of the external magnetic field, time-dependent resistance relaxations, the signatures of the slow glassy dynamics, are observed on the scale of hours, implying the spin-glass character of the 2nd-step transition to zero resistance. Collectively, these findings unveil an unprecedented spin-glass superconducting state and underscore the significant role of low-energy spin fluctuations in the ambient-pressure bilayer nickelate superconductors, providing a critical guidance for the future experimental and theoretical investigations.

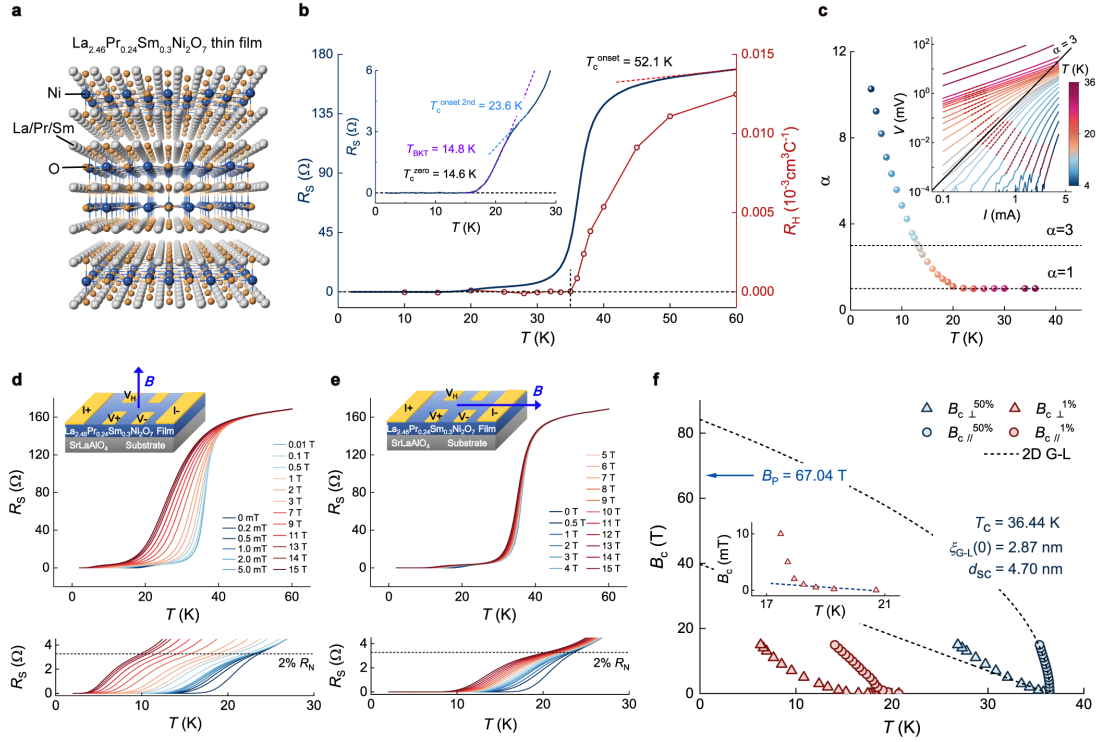


Fig. 1 | Superconductivity in bilayer nickelate $\text{La}_{2.46}\text{Pr}_{0.24}\text{Sm}_{0.3}\text{Ni}_2\text{O}_7$ thin film. **a**, Crystal structure of the bilayer nickelate $\text{La}_{2.46}\text{Pr}_{0.24}\text{Sm}_{0.3}\text{Ni}_2\text{O}_7$ film grown on (001)- SrLaAlO_4 substrate. **b**, Temperature-dependent sheet resistance $R_S(T)$ curve (left axis) and Hall coefficient $R_H(T)$ curve (right axis). $R_H(T)$ drops to zero around 35 K, as indicated by the vertical black dash line. $T_c^{\text{onset}} = 52.1 \text{ K}$ and $T_c^{\text{onset 2nd}} = 23.6 \text{ K}$ are defined by deviation from the extrapolation of the normal state (red dash line) and the $R_S(T)$ step around 25 K (blue dash line in the Inset), respectively. Inset shows the enlarged view of $R_S(T)$ curve, exhibiting a zero-resistance transition at $T_c^{\text{zero}} = 14.6 \text{ K}$, below which the sheet resistance reaches zero within the noise level of the measurement system. Purple dash line represents the fit curve for Berezinskii-Kosterlitz-Thouless (BKT) transition, yielding a BKT temperature $T_{\text{BKT}} = 14.8 \text{ K}$. **c**, Temperature-dependent α determined by $V \sim I^\alpha$. With increasing temperatures, α drops to 3 at T_{BKT} . Inset: $V-I$ curves from 4 K to 36 K. Red dash lines correspond to the power-law dependence $V \sim I^\alpha$. Black solid line marks $\alpha = 3$. **d, e**, Main panels show the $R_S(T)$ curves under out-of-plane magnetic fields (B_\perp , d), and in-plane magnetic fields (B_\parallel , e). Bottom panels zoom-in the second-step transition, which occurs below approximately 2% R_N (black dash lines). Insets show the measurement configurations with Hall bar geometry. **f**, Temperature-dependent $B_c(T)$ for the 1st (blue symbols, using 50%- R_N criterion) and 2nd (red symbols, using 1%- R_N criterion) superconducting phases along out-of-plane (triangles) and in-plane (circles) directions. Dash lines are the 2D Ginzburg-Landau (G-L) fittings of the $B_c(T)$ near T_c . Blue arrow marks the Pauli limit,

$B_p = 67.04$ T, estimated by B_p (in Tesla) = $1.84T_c$ (in Kelvin)²⁹. Inset shows the zoomed-in view of $B_{c\perp}$ ^{1%}.

Two-step superconducting transition

The R-P bilayer nickelate (La, Pr, Sm)₃Ni₂O₇ has a stacking structure of (La, Pr, Sm)O-NiO₂-(La, Pr, Sm)O-NiO₂-(La, Pr, Sm)O, as schematically shown in Fig. 1a. The pure-phase single-crystal (La, Pr, Sm)₃Ni₂O₇ films are grown on treated (001)-oriented SrLaAlO₄ substrates by gigantic-oxidative atomic layer-by-layer epitaxy (GOALL-Epitaxy)^{5,30}. A stoichiometry precision better than 1% is achieved, and the epitaxial strain is coherently maintained within the three-unit-cell (3UC) thickness. The in-plane lattice constant of bulk La_{2.85}Pr_{0.15}Ni₂O₇ is ~ 3.832 Å, so that the thin films grown on (001)-oriented SrLaAlO₄ substrate (3.75 Å) experience a compressive strain of roughly 2%. It is suggested that the short in-plane lattice constant (i.e., short in-plane Ni-O bond length) is crucial for the ambient-pressure superconductivity in the bilayer nickelates^{6,31}.

For the electrical transport measurement, we use the standard electrodes with Hall bar geometry, as schematically shown in the insets of Fig. 1d-e. To start with, the temperature-dependent sheet resistance $R_s(T)$ curve of a 3UC La_{2.46}Pr_{0.24}Sm_{0.3}Ni₂O₇ thin film on SrLaAlO₄ substrate is measured, which shows a superconducting transition with a two-step resistive drop (Fig. 1b). It should be mentioned that all critical results are consistently reproduced in a La_{2.85}Pr_{0.15}Ni₂O₇ film, which are shown in the Extended Data. The onset of the superconducting transition in La_{2.46}Pr_{0.24}Sm_{0.3}Ni₂O₇ thin film occurs around $T_c^{\text{onset}} = 52.1$ K, which is defined by the deviation from the extrapolation of $R_s(T)$ in the normal state. The onset of second-step transition occurs at $T_c^{\text{onset 2nd}} = 23.6$ K, defined by the deviation from the extrapolation of $R_s(T)$ step around 25 K. The zero-resistance within the measurement resolution is achieved at $T_c^{\text{zero}} = 14.6$ K (Inset of Fig. 1b). The $R_s(T)$ curve shows a smooth tail before reaching the zero-resistance state, which is described by the Berezinskii-Kosterlitz-Thouless (BKT) transition in two dimensions^{32,33}. Theoretical fitting to the $R_s(T)$ curve with the Halperin-Nelson equation³⁴ yields a transition temperature $T_{\text{BKT}} = 14.8$ K (Inset of Fig. 1b). Complementary confirmation of the BKT transition is provided by the voltage-current (V - I) curves, where a power-law dependence $V \sim I^\alpha$ is observed (Inset of Fig. 1c). The extracted exponent α increases rapidly with decreasing temperature, and approaches the value of 3 at 13.1 K, yielding a consistent T_{BKT} (Fig. 1c). Figure 1b also shows the temperature-dependent Hall coefficient $R_H(T)$. The small absolute value of R_H in the normal state at 60 K is consistent with the multiband nature at the Fermi level^{5,23}. The

$R_H(T)$ drops sharply when entering the onset of superconducting transition, and reaches zero at around 35 K, which demonstrates the establishment of particle-hole symmetry in the superconducting (SC) state.

To further elucidate the SC dimensionality of the $\text{La}_{2.46}\text{Pr}_{0.24}\text{Sm}_{0.3}\text{Ni}_2\text{O}_7$ films, $R_s(T)$ curves are measured with different out-of-plane (Fig. 1d) and in-plane (Fig. 1e) magnetic fields. For convenience, we denote the phases below the two onsets of the two-step transition as 1st and 2nd SC phase. Compared with the in-plane magnetic field B_{\parallel} , the out-of-plane field B_{\perp} exhibits a stronger suppression on both the 1st and 2nd SC phases, showing the strong SC anisotropy. Particularly, the 2nd phase is highly sensitive to B_{\perp} , so that B_{\perp} as weak as 0.2 mT could induce an apparent change in the $R_s(T)$ curve. The temperature-dependent critical magnetic fields along these orientations ($B_{c\perp}$ and $B_{c\parallel}$) for both the 1st and 2nd SC phases are determined, as shown in Fig. 1f, which are defined as the magnetic fields required to reach 50% and 1% of the normal state sheet resistance R_N , respectively. For the 1st SC phase, $B_{c\perp}^{50\%}$ is linear in T , while $B_{c\parallel}^{50\%}$ scales as $(T_c - T)^{0.5}$, consistent with the phenomenological Ginzburg-Landau (G-L) formula³⁵ for 2D superconductors (dash lines in Fig. 1f). The 2D G-L fit yields a zero-temperature G-L coherence length $\xi_{\text{G-L}}(0) = 2.87$ nm and a SC thickness $d_{\text{sc}} = 4.70$ nm. For the 2nd phase, $B_{c\perp}^{1\%}$ is dramatically small at relatively high temperatures, reflecting the high sensitivity to B_{\perp} . The large difference between $B_{c\perp}^{1\%}$ and $B_{c\parallel}^{1\%}$ is in accord with the strong anisotropy for 2D superconductivity. It is noted that both $B_{c\perp}^{1\%}$ and $B_{c\parallel}^{1\%}$ are non-linear, and show upward curvatures near $T_c^{\text{onset } 2^{\text{nd}}}$ with decreasing temperature, indicating the two-band superconductivity³⁶⁻³⁸ in line with the multi-orbital nature of the bilayer nickelate film²⁵⁻²⁸.

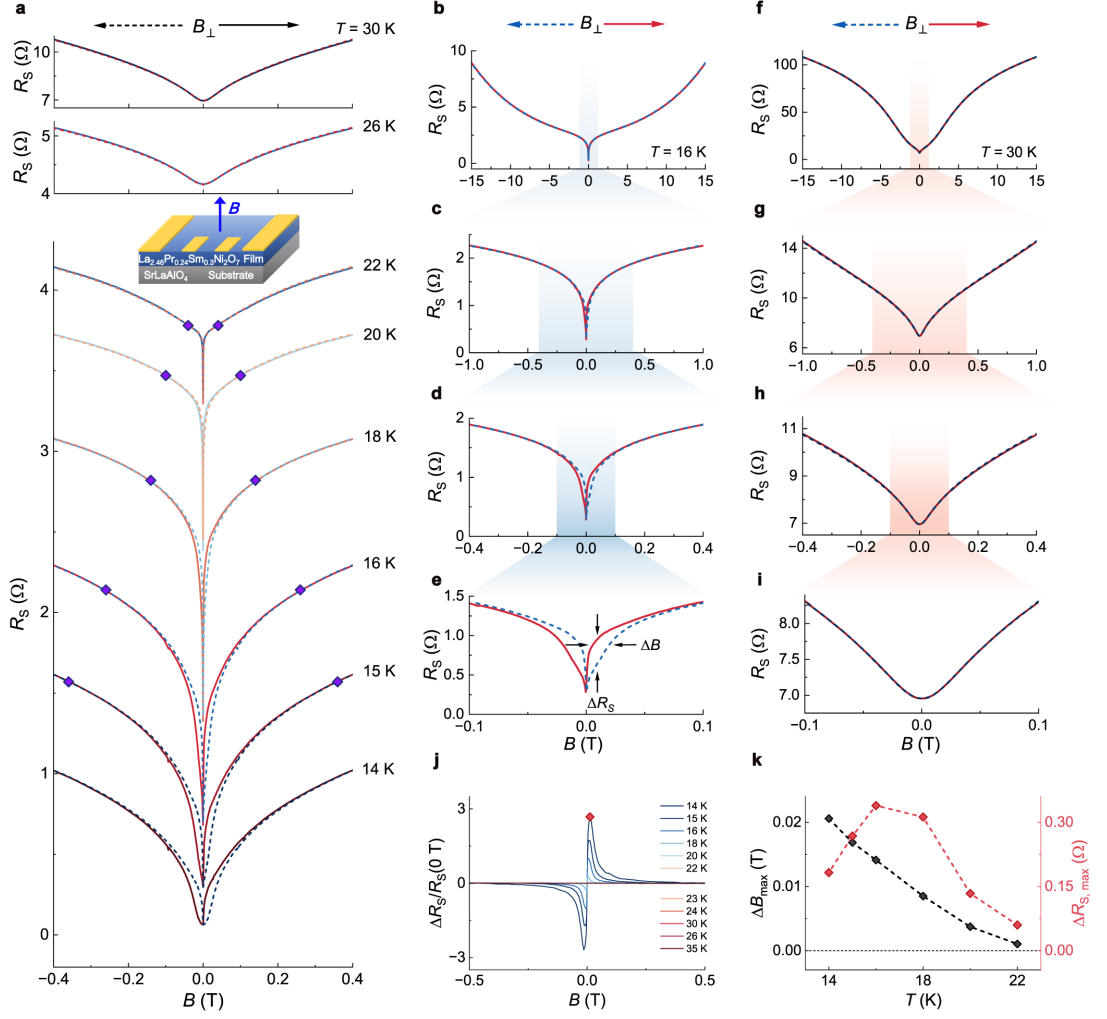


Fig. 2 | Hysteretic magnetoresistance in $\text{La}_{2.46}\text{Pr}_{0.24}\text{Sm}_{0.3}\text{Ni}_2\text{O}_7$ thin film under out-of-plane magnetic fields. **a**, Magnetoresistance $R_s(B)$ curves at different temperatures, zoomed-in to $|B_\perp| \leq 0.4$ T. Curves are offset vertically for clarity. Here, all $R_s(B)$ curves are measured with B_\perp sweeping from 15 T to -15 T (dash lines) and -15 T to 15 T (solid lines), while the selected ranges of $R_s(B)$ curves are displayed for clarity. The hysteresis is observed below 23 K and disappears at higher temperatures. Purple diamonds indicate the saturation fields. Inset shows the measurement configuration. **b-e**, Representative $R_s(B)$ curves from **a** at $T = 16$ K with B_\perp ranging within 15 T (**b**), 1.0 T (**c**), 0.4 T (**d**), 0.1 T (**e**), which show the prominent hysteretic loop. Black arrows schematically mark the ΔB and ΔR , respectively. **f-i**, Representative $R_s(B)$ curves at $T = 30$ K within 15 T (**f**), 1.0 T (**g**), 0.4 T (**h**), 0.1 T (**i**), where no hysteresis loop could be distinguished. The shadows denote the zoomed-in ranges. **j**, $\Delta R_s(B)$ curves, derived by $R_s^\uparrow(B) - R_s^\downarrow(B)$, normalized by $R_s(B = 0 \text{ T})$. One representative $\Delta R_s(B)$ peak to determine $\Delta R_{s, \max}$ (red diamond) is marked. **k**, Temperature-dependent ΔB_{\max} (left axis), and $\Delta R_{s, \max}$ (right axis).

Hysteresis in magnetoresistance under out-of-plane magnetic fields

Remarkably, under out-of-plane magnetic field B_{\perp} sweeping along the opposite directions, an evident hysteretic loop is observed in the magnetoresistance $R_s(B)$ curves of the 2nd SC phase (Fig. 2a). Figures 2b-e show the representative $R_s(B)$ curves obtained by sweeping B_{\perp} at 16 K, with progressively zoomed-in views. Two branches of the $R_s(B)$ curves, measured with magnetic fields sweeping from 15 T to -15 T (blue dash line) and -15 T to 15 T (red solid line), overlap with each other when the magnetic field strength is above 0.26 T (Fig. 2b to d). However, the two branches diverge and manifest a distinct hysteresis loop within approximately $|B_{\perp}| \leq 0.26$ T (Fig. 2c to e). Furthermore, each branch of $R_s(B)$ curve is evidently asymmetric with respect to $B_{\perp} = 0$ T. Such a history-dependent magnetoresistance behavior, irreversible under the time-reversal operation, directly demonstrates the spontaneous TRS breaking. With increasing temperatures, the hysteresis loop shrinks, and then vanishes above 23 K (Fig. 2a, see also Supplementary Information Fig. S2 and Fig. S3 for detailed examinations). The saturated fields, defined as the coincident points of the two branches (indicated by purple diamonds in Fig. 2a), decreases gradually with increasing temperature and becomes indistinguishable above 23 K. Representative $R_s(B)$ curves at 30 K are shown in Fig. 2f-i, where the two branches show no discernable difference, even when zooming-in down to 0.1 T, confirming the absence of hysteresis in the 1st SC phase. These results indicate that the TRS is broken solely in the 2nd SC phase. It should be emphasized that the magnetic fields are calibrated by a high-resolution InAs Hall sensor, which precludes the extrinsic issues such as the remanent field of the measurement system, and thereby demonstrates the intrinsic nature of the hysteretic behaviors (Extended Data Fig. 2).

To quantitatively analyze the hysteresis, we define the displacements of the two sweeping branches (\uparrow from -15 T to 15 T, and \downarrow in reverse) of the magnetoresistance $R_s(B)$ curves: $\Delta R_s(B) = R_s^{\uparrow}(B) - R_s^{\downarrow}(B)$, representing the vertical “height” of the hysteresis loop at a given B (as schematically marked by vertical arrows in Fig. 2e). The normalized $\Delta R_s(B)/\Delta R_s(0 \text{ T})$ plotted as a function of B at different temperatures reveals the field-dependence and the temperature evolution of the hysteresis (Fig. 2j). At different temperatures, a maximum value of $\Delta R_{s,\text{max}}$ can be identified by the peak (one representative peak is marked by the diamond in Fig. 2j). The $\Delta R_{s,\text{max}}$ vanishes when approaching 23 K (Fig. 2k), indicating that the hysteretic behavior is confined to the 2nd SC phase. In a similar vein, the magnetic field difference ΔB are defined, which

depict the horizontal displacements of the hysteresis (as schematically illustrated in Fig. 2e). The extracted maximal amplitude of the hysteretic behavior $\Delta R_{S,\max}$ exhibits an intriguing temperature evolution analogous to an order parameter: it emerges around 23 K, increases monotonically with decreasing temperatures (Fig. 2k). These quantitative results further substantiate that the hysteretic behaviors in magnetoresistance are confined to the 2nd SC phase.

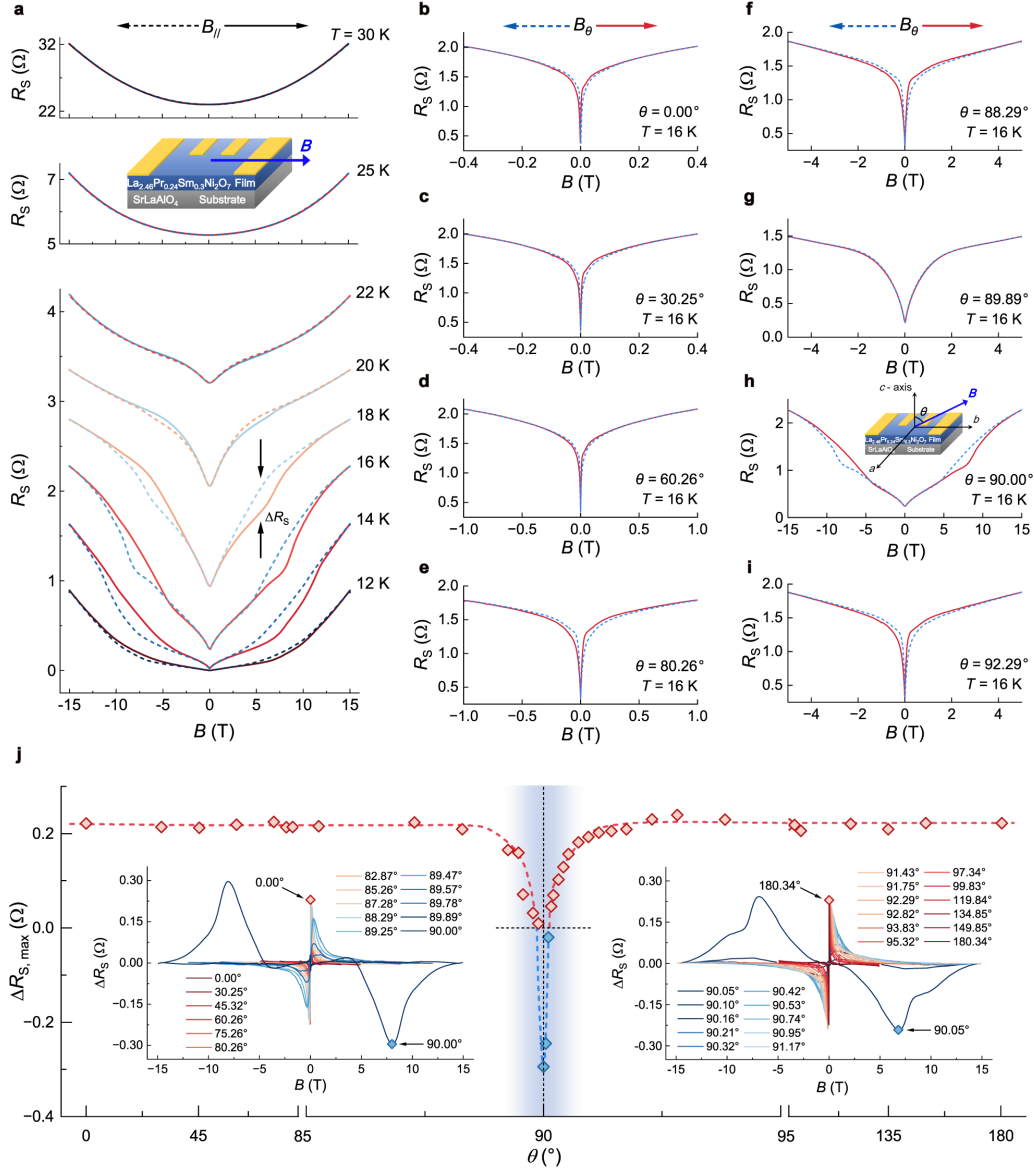


Fig. 3 | Hysteretic magnetoresistance in $\text{La}_{2.46}\text{Pr}_{0.24}\text{Sm}_{0.3}\text{Ni}_2\text{O}_7$ thin film under magnetic fields along different orientations. a, Magnetoresistance $R_S(B)$ curves at different temperatures with B_{\parallel} sweeping from 15 T to -15 T (dash lines) and -15 T to 15 T (solid lines). The hysteresis is observed below 22 K and disappears at higher temperatures. Inset shows the measurement configuration with the voltage electrodes

on the upper area of the film. **b-i**, Representative $R_s(B)$ curves at $T = 16$ K with the opposite swept magnetic fields B_θ along different polar angles θ from 0° (out-of-plane) to 90° (in-plane), and then to higher degrees, as denoted in the figures. **j**, θ -dependence of $\Delta R_{s, \max}$. Red and blue colors highlight the positive and negative polarities. Blue area and dash lines are guides to the eye. Insets show the anti-symmetrized $\Delta R_s(B)$ curves at different θ angles, from which the $\Delta R_{s, \max}$ are determined. Four typical $\Delta R_{s, \max}$ are marked, at 0.00° and 180.34° (positive values, defined as positive polarity, red diamonds), 90.00° and 90.05° (negative values, defined as negative polarity, blue diamonds). The resolution of θ is around 0.05° .

Anisotropic hysteresis under different magnetic field orientations

Interestingly, the hysteretic loop is also observed under an in-plane magnetic field B_{\parallel} in the 2nd SC phase. As shown in Fig. 3a, the two branches of $R_s(B)$ split markedly under B_{\parallel} and exhibit the evident hysteretic behavior, when sweeping the in-plane magnetic fields along opposite directions. Below 18 K, the hysteresis loop seems to be unsaturated up to 15 T (the maximum applied field). This behavior suggests a large saturated field along in-plane orientation, substantially exceeding the out-of-plane value, which indicates the strong anisotropy of the magnetoresistance hysteresis. With increasing temperatures, the hysteresis loop under B_{\parallel} shrinks and then vanishes above 22 K, in good qualitative agreement with the temperature-dependent disappearance of hysteresis under B_{\perp} . As shown in the upper panels in Fig. 3a, no hysteresis loop is detected at 25 K and 30 K. We note that, considering the absence of B_{\parallel} -induced vortices due to confined dimensionality in $\text{La}_{2.46}\text{Pr}_{0.24}\text{Sm}_{0.3}\text{Ni}_2\text{O}_7$ thin films, the hysteresis under B_{\parallel} cannot be attributed to the trapped vortices. Therefore, the exclusive emergence of hysteresis in the 2nd transition under both B_{\perp} and B_{\parallel} demonstrates it as an intrinsic feature of the 2nd SC phase.

To characterize the magnetic field orientation-dependent hysteresis anisotropy, the magnetoresistances are measured under the opposite sweeping magnetic fields B_θ at different polar angles θ from 0.00° (out-of-plane, Fig. 3b) to 90.00° (in-plane, Fig. 3h), and then to higher degrees (Fig. 3i). As θ increases from 0.00° to 88.29° , the hysteresis loop expands and the saturated field increases. This trend may be associated with the diminished B_{\perp} -component that is proportional to $\cos \theta$. However, when θ further increases, the hysteresis loop undergoes an abnormal evolution: it significantly shrinks and nearly closes at 89.89° , and then fully re-opens around 90.00° with a reversed polarity. This abrupt change with polarity reversal within a narrow θ range around

90.00° (in-plane) cannot be attributed to the effect of a B_{\perp} -component.

To comprehensively depict the θ -dependent hysteresis, the ΔR_S versus B curves at different θ are extracted at 16 K (inset of Fig. 3j), and the θ -dependent $\Delta R_{S, \max}$ are determined (Fig. 3j). With increasing θ from 0° to approximately 88°, the $\Delta R_{S, \max}(\theta)$ values remain around 0.22 Ω , showing a weak θ -dependence. With θ is further increased from 88° to 90°, the $\Delta R_{S, \max}(\theta)$ decreases rapidly from a positive 0.22 Ω (red diamonds), goes through zero (0 Ω marked by black dash line), and then reaches negative 0.29 Ω (blue diamond). With increasing θ from 90° to 180°, $\Delta R_{S, \max}$ exhibits a mirror symmetric θ -dependence compared to $\Delta R_{S, \max}(\theta)$ from 0° to 90° about $\theta = 90^\circ$. The rapid decrease and sign change of $\Delta R_{S, \max}(\theta)$ within 1° quantitatively illustrate the abrupt change of the hysteresis loop, which cannot be explained by the B_{\perp} -component and the induced vortices. The overall θ -dependent $\Delta R_{S, \max}$ is centered at $\theta = 90^\circ$, confirming the intrinsic nature of the rapid change, which cannot be ascribed to misalignment of θ . The singular θ -dependence confined within a small angle is reminiscent of the interlayer Josephson coupling in layered superconductors under in-plane magnetic field³⁹⁻⁴². Further investigations focusing on this confined θ -range are required to elucidate the underlying microscopic origin.

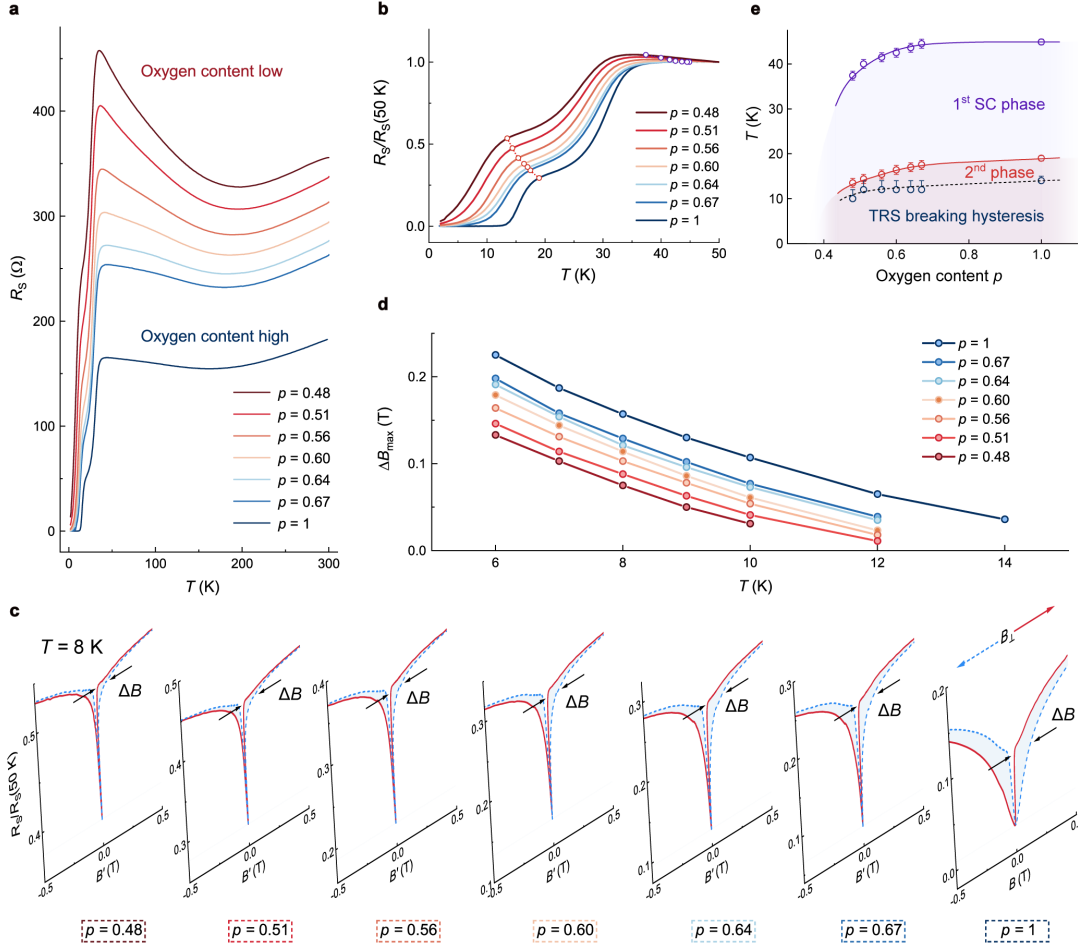


Fig. 4 | Oxygen-content modulation of superconductivity and hysteresis in $\text{La}_{2.85}\text{Pr}_{0.15}\text{Ni}_2\text{O}_7$ thin film. **a**, $R_S(T)$ curve for one $\text{La}_{2.85}\text{Pr}_{0.15}\text{Ni}_2\text{O}_7$ thin film with different oxygen contents. **b**, Normalized $R_S(T)/R_S(T = 50 \text{ K})$ curves, reproduced from **a**. Purple and red circles mark the T_c^{onset} and $T_c^{\text{onset 2nd}}$, respectively. **c**, Normalized magnetoresistance $R_S(B, T = 8 \text{ K})/R_S(B = 0 \text{ T}, T = 50 \text{ K})$ at different oxygen contents. Blue areas highlight the hysteresis. Black arrows schematically mark ΔB of the hysteresis. **d**, Extracted ΔB_{max} of the hysteresis as a function of temperature for different oxygen contents. **e**, Phase diagram as a function of temperature T and oxygen content p , incorporating the onset boundaries of 1st-step superconducting transition, 2nd phase transition, and TRS breaking hysteresis. Error bars represent the temperature intervals during the measurements. Solid lines are guides to the eyes. Here, oxygen content p is determined by $p = 157.3 \text{ } \Omega / R_S(T = 200 \text{ K})$.

Oxygen content-dependence of hysteresis

To dig into the microscopic origin of the hysteresis, we modulate the oxygen content p in a $\text{La}_{2.85}\text{Pr}_{0.15}\text{Ni}_2\text{O}_7$ thin film and track the evolution of hysteresis with oxygen loss.

The bilayer nickelate $\text{La}_{2.85}\text{Pr}_{0.15}\text{Ni}_2\text{O}_7$ film with $p = 1$ exhibits a two-step SC transition with $T_c^{\text{onset}} = 44.9$ K, $T_c^{\text{onset } 2^{\text{nd}}} = 19.0$ K, and $T_c^{\text{zero}} = 7.8$ K (dark blue curve in Fig. 4a). Qualitatively consistent with the $\text{La}_{2.46}\text{Pr}_{0.24}\text{Sm}_{0.3}\text{Ni}_2\text{O}_7$ film, hysteretic behaviors of the magnetoresistance with identical characteristics are observed exclusively in the 2nd SC phase in $\text{La}_{2.85}\text{Pr}_{0.15}\text{Ni}_2\text{O}_7$ film. The hysteresis is also observed under both out-of-plane and in-plane magnetic fields, and exhibits a strong anisotropy across different field orientations, confirming the reproducibility of the robust hysteretic behaviors in the SC nickelate thin films (Extended Data Fig. 4 to Fig. 6).

The superconductivity in the bilayer nickelate film is highly sensitive to the oxygen content^{5,6,22}, which offers a practical tuning parameter. By *in situ* modulating the oxygen content (See **Method** for detailed process), the SC properties in one $\text{La}_{2.85}\text{Pr}_{0.15}\text{Ni}_2\text{O}_7$ film with different oxygen contents are characterized (Fig. 4a). Here, the oxygen content p is determined by the empirical relation $p = 157.3 \Omega / R_s(T = 200 \text{ K})$ ^{43,44}, where the initial state with $R_s(T = 200 \text{ K}) = 157.3 \Omega$ is set as $p = 1$. Upon oxygen reduction, the film becomes more resistive, and a strong upturn is manifested in the $R_s(T)$ curves before entering the SC transitions (Fig. 4a). Simultaneously, the superconductivity is gradually weakened, as demonstrated by the comparison of the normalized $R_s(T)/R_s(T = 50 \text{ K})$ shown in Fig. 4b. Figure 4c displays the normalized magnetoresistance $R_s(B, T = 8 \text{ K})/R_s(B = 0 \text{ T}, T = 50 \text{ K})$ measured with different p values, revealing that the magnetoresistance hysteresis shrinks progressively with reduced oxygen content. Defining a “width” of the hysteresis ΔB as schematically marked in Fig. 4c, the magnitude of the hysteresis can be qualitatively described by maximum horizontal displacement ΔB_{max} at a given temperature. Extracting $\Delta B_{\text{max}}(T)$ for each oxygen content p , the temperature evolution of the hysteresis amplitude at different values of p is plotted in Fig. 4d. Overall, ΔB_{max} decays with increasing temperatures, consistent with the confinement of the hysteretic behavior to the 2nd SC phase. Importantly, a systematic descending trend of ΔB_{max} with reduction of the oxygen content p at all different temperatures further supports the suppression of the hysteresis with oxygen reduction (Fig. 4d). Summarizing the temperature- and the p -dependences, Figure 4e shows a phase diagram, where all the onset boundaries for the 1st-step and the 2nd-step SC transition, and the TRS breaking hysteretic behavior are suppressed with reduced oxygen content.

The observed correlation of the hysteretic behavior with the oxygen loss offers valuable insights into the orbital content of the hysteresis. Recently, orbital reconfiguration driven by the oxygen reduction was reported²⁶. The dominance of the spectral weight

of the $\text{Ni-}3d_{x^2-y^2}$ orbital near the Fermi level is progressively replaced by that of the $\text{Ni-}3d_{z^2}$ orbital upon oxygen reduction. Taking together, the current finding offers an intriguing result that the microscopic origin of the hysteretic TRS breaking phase may be predominantly related to the $\text{Ni-}3d_{x^2-y^2}$ orbital.

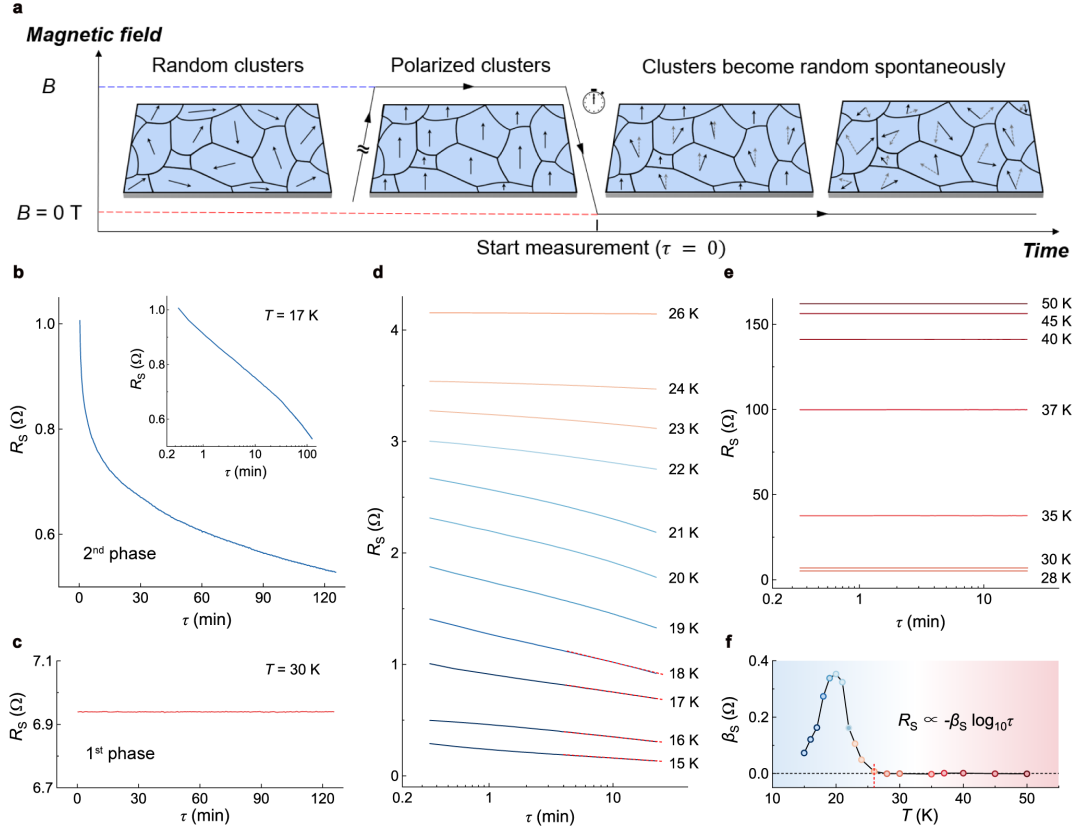


Fig. 5 | Time-dependent resistance relaxations in $\text{La}_{2.46}\text{Pr}_{0.24}\text{Sm}_{0.3}\text{Ni}_2\text{O}_7$ thin film.

a, Schematic illustration of the measurement process. At a fixed temperature, an external magnetic field, exceeding the saturated field of the hysteresis, is applied to fully polarize the random glass clusters. Then, the external magnetic field is reduced to zero. Upon reaching zero field, the time-dependent resistance measurements initiate at the counting time $\tau = 0$. **b**, Time-dependent sheet resistance $R_s(\tau)$ at 17 K, exhibit a gradual decrease over time. Inset: $R_s(\tau)$ from **b** plotted on logarithmic time scale. **c**, $R_s(\tau)$ at 30 K, remaining basically invariant over time. **d**, $R_s(\tau)$ below 26 K, showing nearly logarithmic time-dependent resistance relaxation. **e**, $R_s(\tau)$ above 26 K, showing no discernable time-dependent variation. **f**, Temperature-dependence of the relaxation exponent β , extracted from $R_s \propto -\beta \log_{10} \tau$. Red dash lines in **d** are the fit curves to

extract β .

Logarithmically slow resistance relaxation

The coalescing resistance minima at zero magnetic field in the magnetoresistance hysteresis suggest an unusual origin for the hysteretic behaviors, in sharp contrast to the presence of long-range ferromagnetic order where they would be split by the coercive field⁴⁵⁻⁴⁷. To gain further insight into the TRS breaking state at zero magnetic field, we investigate the time-dependent zero-field sheet resistance $R_s(\tau)$, after the application and removal of the external field. The measurement process is schematically illustrated in Fig. 5a. To start with, an external magnetic field, which exceeds the saturated field of the hysteresis, is applied to fully polarize the (La, Pr, Sm)₃Ni₂O₇ film. The external magnetic field is then removed. Upon reaching zero field, the time-dependent resistance measurement is initiated at the counting time $\tau = 0$. Figure 5b shows one representative $R_s(\tau)$ curve for La_{2.46}Pr_{0.24}Sm_{0.3}Ni₂O₇ thin film at 17 K, which is below $T_c^{\text{onset } 2^{\text{nd}}}$. The $R_s(\tau)$ curve shows a slow but evident time-dependent decrease, with no saturating tendency over 120 minutes, which could be better visualized by the nearly logarithmic time-dependence (Inset of Fig. 5b). The spontaneous and enduring resistance relaxations reveal the logarithmically slow dynamics, which represents the hallmark of a glassy order and is referred to as aging effect in spin glasses^{48,49}. In comparison, the $R_s(\tau)$ curve measured by exactly the same procedure at 30 K, which is slightly above $T_c^{\text{onset } 2^{\text{nd}}}$ and outside the hysteretic magnetoresistance region, remains invariant over time, indicating the absence of glassy dynamics in the 1st-step SC phase (Fig. 5c).

The relation between glassy dynamics and 2nd phase is further illuminated by the $R_s(\tau)$ curves at different temperatures, where the $R_s(\tau)$ curves below 26 K show evident time-dependent decreases (Fig. 5d), while the $R_s(\tau)$ curves above 26 K are time-independent (Fig. 5e). Furthermore, the exponents of the time-dependence can be approximately extracted by fitting with $R_s \propto -\beta \log_{10} \tau$ at different temperatures (representative fit curves are shown by red dash lines in Fig. 5d). Fig. 5f displays the temperature evolution of the exponent β , which is non-zero below 26 K, and vanishes above 26 K, suggesting an onset of spin freezing into a glassy state around 26 K.

The consistent $R_s(\tau)$ relaxations in the 2nd phase are reproduced in La_{2.85}Pr_{0.15}Ni₂O₇ film with $p = 0.48$, whose 2nd transition emerges around 13.5 K, reinforcing the correlation

between the glassy nature and the 2nd phase (Extended Data Fig. 7). It is noted that the $\text{La}_{2.85}\text{Pr}_{0.15}\text{Ni}_2\text{O}_7$ film with $p = 0.48$ was measured in another measurement system, which further confirms the intrinsic feature of the $R_S(\tau)$ relaxations. Particularly, the $R_S(\tau)$ relaxations show stronger variations with the faster removal of polarizing magnetic fields to zero (Extended Data Fig. 8b). This is reminiscent of the cooling rate-dependence in the spin-glass aging effect⁵⁰. Therefore, the observed time-dependent resistance relaxations are highly suggestive of an emergent glass order, which may account for the 2nd phase transition, and contribute to the unconventional SC behaviors.

Discussion

Before discussing the potential origin of the observed TRS breaking SC phase with glassy dynamics in $(\text{La}, \text{Pr}, \text{Sm})_3\text{Ni}_2\text{O}_7$ films, we first rule out several “extrinsic” mechanisms. First of all, we emphasize that all main experimental results, including the two-step SC transition, the hysteretic magnetoresistance with coalescing minima and singular θ -dependence, and the slow resistance relaxation, are consistently reproduced in two samples: a $\text{La}_{2.46}\text{Pr}_{0.24}\text{Sm}_{0.3}\text{Ni}_2\text{O}_7$ film and a $\text{La}_{2.85}\text{Pr}_{0.15}\text{Ni}_2\text{O}_7$ film, which is highly suggestive of an intrinsic and universal nature for the hysteretic and glassy-like SC state in the bilayer nickelate films. Second, the remanent magnetic field of the magnet can be excluded, as evidenced by the absence of hysteresis in the 1st-step transition in both $(\text{La}, \text{Pr}, \text{Sm})_3\text{Ni}_2\text{O}_7$ films, and in a controlled conventional superconductor Nb film (Extended Data Fig. 9). Moreover, the magnetic fields are calibrated by a high-resolution InAs Hall sensor (Extended Data Fig. 2). Third, the trapped vortices scenario is excluded, since the hysteresis is also observed under in-plane magnetic fields, where the field-induced vortices should not exist due to the confined dimensionality. Furthermore, the $R_S(B)$ curves under opposite sweeping out-of-plane magnetic fields exhibit coalescing minima at 0 T (also confirmed by the Hall sensor). This is fundamentally against the scenario of trapped vortices⁵¹, in which two sharply split minima emerge at symmetric magnetic fields, resultant from the cancellation between the trapped flux and the applied magnetic field. Fourth, magnetic impurities are unlikely (note that all measurement components are non-magnetic, including the SrLaAlO_4 substrates, Pt electrodes, and Al wires). Otherwise, the signals of hysteretic magnetoresistance should be equally detected in the 1st-step SC phase. Fifth, the systematic oxygen-content dependence of the hysteresis pins down the involvement of electronic orbitals of Ni and O, precluding the extrinsic possibilities such as vortex dynamics and magnetic impurities (including the rare-earth elements La, Pr, Sm). The detailed discussions on excluding the “extrinsic” TRS breaking are elaborated in the extended discussion in **Methods**.

Our key findings comprise the TRS breaking hysteretic magnetoresistance with coalescing minima, the correlation of the hysteresis with the electronic orbitals modulated by oxygen content, and the logarithmically slow resistance relaxation. These experimental observations consistently point to the emergence of a spin-glass order in coexistence with superconductivity. Despite the absence of long-range magnetic order in the superconducting nickelates, short-range magnetic correlations and spin dynamics indicative of a spin-glass phase have been reported in the infinite layer nickelate films $R\text{NiO}_2$ ⁵²⁻⁵⁴ and trilayer nickelate bulks $\text{Pr}_4\text{Ni}_3\text{O}_8$ ⁵⁵. Moreover, spin density wave correlations have been identified in the bulk bilayer nickelate $\text{La}_3\text{Ni}_2\text{O}_7$ recently⁵⁶⁻⁵⁸. Under high pressure, the static long-range magnetic order is suppressed, and the superconductivity arises⁵⁹. In the ambient-pressure superconducting bilayer nickelate $(\text{La}, \text{Pr}, \text{Sm})_3\text{Ni}_2\text{O}_7$ thin films studied here, it is conceivable that the short-range magnetic correlations and fluctuations may contribute to the unconventional SC pairing, and freeze into a spin-glass phase with randomly distributed clusters, manifesting the 2nd-step SC transition as observed. The slow spin-glass dynamics governing aging naturally accounts for the logarithmically slow resistance relaxations observed at zero field from a field-polarized state.

The emergence of the low-temperature spin-glass phase consistently captures the observed hysteretic magnetoresistance behavior confined to the 2nd transition. The external magnetic field aligns the magnetic moment of the spin cluster irreversibly, modulating the scattering rate and generating the memory effect in the magnetoresistance. The spatially disordered glassy magnetic moments at zero magnetic field may account for the coalescing magnetoresistance minima, in contrast to two sharply split dips due to the coercivity in long-range-ordered magnetism. Furthermore, the hysteresis observed under both out-of-plane and in-plane magnetic fields supports an electron spin origin of glassy state associated with the Ni-3*d* orbitals. This picture is further supported by the observed correlation between the hysteretic behavior and the oxygen content.

It is useful to compare and contrast with the high- T_c cuprate superconductors that motivate the search and exploration of the nickelate superconductors. The undoped cuprates are antiferromagnetic ordered *p-d* charge-transfer insulators, where the spin-1/2 magnetic moments arise from the half-filled Cu 3*d*_{*x*²-*y*²} orbital. Hole doping effectively leads to a less than half-filled single-band derived from Cu 3*d*_{*x*²-*y*²} and in-

plane O $2p_{x,y}$ orbitals⁶⁰, while the fully occupied Cu $3d_{z^2}$ orbital lies well below the Fermi level. Holes on oxygen sites combine with the $3d_{x^2-y^2}$ spins to form the Zhang-Rice singlets⁶¹, destroying the long-range antiferromagnetic order rapidly. Remarkably, a spin-glass phase emerges with frozen Cu spin of the strongly correlated $3d_{x^2-y^2}$ orbital⁶²⁻⁶⁶, which fades away as the superconductivity setting in. In contrast, the bilayer nickelates are $p-d$ charge transfer metals, where both the correlated Ni $3d_{z^2}$ and $3d_{x^2-y^2}$ orbitals are involved at the Fermi level, and produce a multi-band superconductivity. Thus, an electron spin origin for the detected glassy state is quite likely in our superconducting bilayer nickelates (La, Pr, Sm)₃Ni₂O₇ films.

Intriguingly, the observed positive correlation between the hysteresis and the oxygen content indicates that the magnetic moment is dominated by the contributions from the Ni $3d_{x^2-y^2}$ orbital, since it has been observed recently that the oxygen loss enhances the Ni $3d_{z^2}$ orbital contribution at low energies along with weakened superconductivity in the bilayer nickelate films²⁶. Moreover, the dependence of the spin-glass phase on the oxygen content, as that of superconductivity itself, suggests that its emergence cannot be ascribed to inhomogeneity or disorder, but is rather related to electronic orbital-dependent exchange correlations in the multi-orbital nickelates. It is noteworthy that both the oxygen-content dependence and the temperature evolution at a fixed oxygen composition consistently support the positive correlation between the superconducting and spin-glass orders, which is distinct from the cuprate⁶⁵ and the infinite-layer nickelate⁵⁴.

These similarities and distinctions between the nickelates and cuprates may provide complementary insights into the magnetic correlations and the unconventional high- T_c superconductivity in the multi-orbital nickelates and the single-orbital cuprates. While the microscopic mechanism for the emergence of the spin-glass order and the spin-glass SC state remains elusive in both materials, the unprecedented TRS breaking SC state with hysteretic behaviors and glassy dynamics discovered here engenders an important and new dimension to the nickelate superconductors that warrants further experimental and theoretical investigations. The observations imply the presence of low-energy spin fluctuations below the superconducting onset temperature, and their freezing into a spin-glass state plays an important role in stabilizing the zero-resistance

superconducting state in bilayer R-P nickelates. Our findings collectively provide the phenomenological and conceptual advances to the understanding of electron orbitals, magnetic correlations, spin dynamics, and the unconventional superconductivity in the ambient-pressure high- T_c nickelate superconductors.

References

1. Sun, H. L. *et al.* Signatures of superconductivity near 80 K in a nickelate under high pressure. *Nature* **621**, 493 (2023).
2. Hou, J. *et al.* Emergence of High-Temperature Superconducting Phase in Pressurized $\text{La}_3\text{Ni}_2\text{O}_7$ Crystals. *Chin. Phys. Lett.* **40**, 117302 (2023).
3. Zhang, Y. *et al.* High-temperature superconductivity with zero resistance and strange-metal behaviour in $\text{La}_3\text{Ni}_2\text{O}_{7-\delta}$. *Nat. Phys.* **20**, 1269–1273 (2024).
4. Wang, N. *et al.* Bulk high-temperature superconductivity in pressurized tetragonal $\text{La}_2\text{PrNi}_2\text{O}_7$. *Nature* **634**, 579–584 (2024).
5. Zhou, G. *et al.* Ambient-pressure superconductivity onset above 40 K in $(\text{La,Pr})_3\text{Ni}_2\text{O}_7$ films. *Nature* **640**, 641 (2025).
6. Ko, E. K. *et al.* Signatures of ambient pressure superconductivity in thin film $\text{La}_3\text{Ni}_2\text{O}_7$. *Nature* **638**, 935 (2025).
7. Bednorz, J. G. a. K. A. M. Possible high T_c superconductivity in the Ba-La-Cu-O system. *Zeitschrift fr Physik B Condensed Matter* **64**, 189-193 (1986).
8. Wu, M. K. *et al.* Superconductivity at 93 K in a new mixed-phase Y-Ba-Cu-O compound system at ambient pressure. *Phys. Rev. Lett.* **58**, 908-910 (1987).
9. Maeno, Y. *et al.* Superconductivity in a layered perovskite without copper. *Nature* **372**, 532-534 (1994).
10. Li, D. *et al.* Superconductivity in an infinite-layer nickelate. *Nature* **572**, 624-627 (2019).
11. Dong, Z. *et al.* Visualization of oxygen vacancies and self-doped ligand holes in $\text{La}_3\text{Ni}_2\text{O}_{7-\delta}$. *Nature* **630**, 847–852 (2024).
12. Luo, Z., Hu, X., Wang, M., Wú, W. and Yao, D.-X. Bilayer Two-Orbital Model of $\text{La}_3\text{Ni}_2\text{O}_7$ under Pressure. *Phys. Rev. Lett.* **131**, 126001 (2023).
13. Liu, Y.-B., Mei, J.-W., Ye, F., Chen, W.-Q. and Yang, F. s^\pm -Wave pairing and the

- destructive role of apical-oxygen deficiencies in $\text{La}_3\text{Ni}_2\text{O}_7$ under pressure. *Phys. Rev. Lett.* **131**, 236002 (2023).
14. Yang, Q.-G., Wang, D. and Wang, Q.-H. Possible s_{\pm} -wave superconductivity in $\text{La}_3\text{Ni}_2\text{O}_7$. *Phys. Rev. B* **108**, L140505 (2023).
 15. Oh, H. and Zhang, Y.-H. Type-II $t - J$ model and shared superexchange coupling from Hund's rule in superconducting $\text{La}_3\text{Ni}_2\text{O}_7$. *Phys. Rev. B* **108**, 174511 (2023).
 16. Wang, M., Wen, H.-H., Wu, T., Yao, D.-X. and Xiang, T. Normal and Superconducting Properties of $\text{La}_3\text{Ni}_2\text{O}_7$. *Chin. Phys. Lett.* **41**, 077402 (2024).
 17. Hu, X., Qiu, W., Chen, C.-Q., Luo, Z. and Yao, D.-X. Electronic structures and multi-orbital models of $\text{La}_3\text{Ni}_2\text{O}_7$ thin films at ambient pressure. Preprint at <http://arxiv.org/abs/2503.17223>.
 18. Lu, C., Pan, Z., Yang, F. and Wu, C. Interlayer-Coupling-Driven High-Temperature Superconductivity in $\text{La}_3\text{Ni}_2\text{O}_7$ under Pressure. *Phys. Rev. Lett.* **132**, 146002 (2024).
 19. Yang, Y.-f., Zhang, G.-M. and Zhang, F.-C. Interlayer valence bonds and two-component theory for high- T_c superconductivity of $\text{La}_3\text{Ni}_2\text{O}_7$ under pressure. *Phys. Rev. B* **108**, L201108 (2023).
 20. Fan, Z. *et al.* Superconductivity in nickelate and cuprate superconductors with strong bilayer coupling. *Phys. Rev. B* **110**, 024514 (2024).
 21. Qu, X.-Z. *et al.* Bilayer t - J - J_{\perp} Model and Magnetically Mediated Pairing in the Pressurized Nickelate $\text{La}_3\text{Ni}_2\text{O}_7$. *Phys. Rev. Lett.* **132**, 036502 (2024).
 22. Liu, Y. *et al.* Superconductivity and normal-state transport in compressively strained $\text{La}_2\text{PrNi}_2\text{O}_7$ thin films. *Nat. Mater.* **24**, 1221–1227 (2025).
 23. Hao, B. *et al.* Superconductivity in Sr-doped $\text{La}_3\text{Ni}_2\text{O}_7$ thin films. *Nat. Mater.* (2025). <https://dx.doi.org/10.1038/s41563-025-02327-2>.
 24. Shen, J. *et al.* Anomalous energy gap in superconducting $\text{La}_{2.85}\text{Pr}_{0.15}\text{Ni}_2\text{O}_7/\text{SrLaAlO}_4$ heterostructures. Preprint at <http://arxiv.org/abs/2502.17831>.
 25. Li, P. *et al.* Angle-resolved photoemission spectroscopy of superconducting $(\text{La},\text{Pr})_3\text{Ni}_2\text{O}_7/\text{SrLaAlO}_4$ heterostructures. *Nat. Sci. Rev.* (2025).

<https://dx.doi.org/10.1093/nsr/nwaf205>.

26. Wang, H. *et al.* Electronic Structures across the Superconductor-Insulator Transition at $\text{La}_{2.85}\text{Pr}_{0.15}\text{Ni}_2\text{O}_7/\text{SrLaAlO}_4$ Interfaces. Preprint at <http://arxiv.org/abs/2502.18068>.
27. Wang, B. Y. *et al.* Electronic structure of compressively strained thin film $\text{La}_2\text{PrNi}_2\text{O}_7$. Preprint at <http://arxiv.org/abs/2504.16372>.
28. Fan, S. *et al.* Superconducting gaps revealed by STM measurements on $\text{La}_2\text{PrNi}_2\text{O}_7$ thin films at ambient pressure. Preprint at <http://arxiv.org/abs/2506.01788>.
29. Clogston, A. M. Upper Limit for the Critical Field in Hard Superconductors. *Phys. Rev. Lett.* **9**, 266-267 (1962).
30. Zhou, G. *et al.* Gigantic-oxidative atomic-layer-by-layer epitaxy for artificially designed complex oxides. *Nat. Sci. Rev.* **12**, nwae429 (2024).
31. Bhatt, L. *et al.* Resolving Structural Origins for Superconductivity in Strain-Engineered $\text{La}_3\text{Ni}_2\text{O}_7$ Thin Films. Preprint at <http://arxiv.org/abs/2501.08204>.
32. Berezinskii, V. L. Destruction of long-range order in one-dimensional and two-dimensional systems having a continuous symmetry group. I. Classical systems. *Sov. Phys. JETP* **32**, 493 (1971).
33. Kosterlitz, J. M. and Thouless, D. J. Ordering, metastability and phase transitions in two-dimensional systems. *J. Phys. C: Solid State Phys.* **6**, 1181-1203 (1973).
34. Halperin, B. I. and Nelson, D. R. Resistive transition in superconducting films. *J. Low Temp. Phys.* **36**, 599-616 (1979).
35. Harper, F. E. and Tinkham, M. The Mixed State in Superconducting Thin Films. *Phys. Rev.* **172**, 441-450 (1968).
36. Hunte, F. *et al.* Two-band superconductivity in $\text{LaFeAsO}_{0.89}\text{F}_{0.11}$ at very high magnetic fields. *Nature* **453**, 903-905 (2008).
37. Li, Y. *et al.* Nontrivial superconductivity in topological $\text{MoTe}_{2-x}\text{S}_x$ crystals. *Proc. Natl. Acad. Sci. USA* **115**, 9503-9508 (2018).
38. Ji, H., Liu, Y., Ji, C. and Wang, J. Two-Dimensional and Interface Superconductivity in Crystalline Systems. *Acc. Mater. Res.* **5**, 1146-1157 (2024).

39. Fuhrer, M. S., Ino, K., Oka, K., Nishihara, Y. and Zettl, A. Observation of Josephson vortex lattice melting in a highly anisotropic superconductor. *Solid State Commun.* **101**, 841-845 (1997).
40. Liu, C.-X. Unconventional Superconductivity in Bilayer Transition Metal Dichalcogenides. *Phys. Rev. Lett.* **118**, 087001 (2017).
41. Wan, P. *et al.* Orbital Fulde–Ferrell–Larkin–Ovchinnikov state in an Ising superconductor. *Nature* **619**, 46-51 (2023).
42. Lin, J. *et al.* Exceedingly large in-plane critical field of finite-momentum pairing state in bulk superlattices. Preprint at <http://arxiv.org/abs/2506.16039>.
43. Bollinger, A. T. *et al.* Superconductor–insulator transition in $\text{La}_{2-x}\text{Sr}_x\text{CuO}_4$ at the pair quantum resistance. *Nature* **472**, 458-460 (2011).
44. Yu, Y. *et al.* High-temperature superconductivity in monolayer $\text{Bi}_2\text{Sr}_2\text{CaCu}_2\text{O}_{8+\delta}$. *Nature* **575**, 156-163 (2019).
45. Brinkman, A. *et al.* Magnetic effects at the interface between non-magnetic oxides. *Nat. Mater.* **6**, 493-496 (2007).
46. Dikin, D. A. *et al.* Coexistence of Superconductivity and Ferromagnetism in Two Dimensions. *Phys. Rev. Lett.* **107**, 056802 (2011).
47. Hua, X. *et al.* Superconducting stripes induced by ferromagnetic proximity in an oxide heterostructure. *Nat. Phys.* **20**, 957–963 (2024).
48. Sompolinsky, H. Time-Dependent Order Parameters in Spin-Glasses. *Phys. Rev. Lett.* **47**, 935-938 (1981).
49. Jonason, K., Vincent, E., Hammann, J., Bouchaud, J. P. and Nordblad, P. Memory and Chaos Effects in Spin Glasses. *Phys. Rev. Lett.* **81**, 3243-3246 (1998).
50. Rodriguez, G. F., Kenning, G. G. and Orbach, R. Full Aging in Spin Glasses. *Phys. Rev. Lett.* **91**, 037203 (2003).
51. Ji, L., Rzchowski, M. S., Anand, N. and Tinkham, M. Magnetic-field-dependent surface resistance and two-level critical-state model for granular superconductors. *Phys. Rev. B* **47**, 470-483 (1993).
52. Lin, H. *et al.* Universal spin-glass behaviour in bulk LaNiO_2 , PrNiO_2 and NdNiO_2 .

- New J. Phys.* **24**, 013022 (2022).
53. Ortiz, R. A. *et al.* Magnetic correlations in infinite-layer nickelates: An experimental and theoretical multimethod study. *Phys. Rev. Res.* **4**, 023093 (2022).
 54. Saykin, D. R. *et al.* Spin-glass state in nickelate superconductors. Preprint at <http://arxiv.org/abs/2506.03262>.
 55. Huangfu, S. *et al.* Short-range magnetic interactions and spin-glass behavior in the quasi-two-dimensional nickelate $\text{Pr}_4\text{Ni}_3\text{O}_8$. *Phys. Rev. B* **102**, 054423 (2020).
 56. Chen, K. *et al.* Evidence of Spin Density Waves in $\text{La}_3\text{Ni}_2\text{O}_{7-\delta}$. *Phys. Rev. Lett.* **132**, 256503 (2024).
 57. Khasanov, R. *et al.* Pressure-enhanced splitting of density wave transitions in $\text{La}_3\text{Ni}_2\text{O}_{7-\delta}$. *Nat. Phys.* **21**, 430–436 (2025).
 58. Chen, X. *et al.* Electronic and magnetic excitations in $\text{La}_3\text{Ni}_2\text{O}_7$. *Nat. Commun.* **15**, 9597 (2024).
 59. Zhao, D. *et al.* Pressure-enhanced spin-density-wave transition in double-layer nickelate $\text{La}_3\text{Ni}_2\text{O}_{7-\delta}$. *Sci. Bull.* **70**, 1239-1245 (2025).
 60. Lee, P. A., Nagaosa, N. and Wen, X.-G. Doping a Mott insulator: Physics of high-temperature superconductivity. *Rev. Mod. Phys.* **78**, 17-85 (2006).
 61. Zhang, F. C. and Rice, T. M. Effective Hamiltonian for the superconducting Cu oxides. *Phys. Rev. B* **37**, 3759-3761 (1988).
 62. Aharony, A., Birgeneau, R. J., Coniglio, A., Kastner, M. A. and Stanley, H. E. Magnetic phase diagram and magnetic pairing in doped La_2CuO_4 . *Phys. Rev. Lett.* **60**, 1330-1333 (1988).
 63. Julien, M. Magnetic order and superconductivity in $\text{La}_{2-x}\text{Sr}_x\text{CuO}_4$: a review. *Phys. B* **329-333**, 693-696 (2003).
 64. Chou, F. C., Belk, N. R., Kastner, M. A., Birgeneau, R. J. and Aharony, A. Spin-Glass Behavior in $\text{La}_{1.96}\text{Sr}_{0.04}\text{CuO}_4$. *Phys. Rev. Lett.* **75**, 2204-2207 (1995).
 65. Niedermayer, C. *et al.* Common Phase Diagram for Antiferromagnetism in $\text{La}_{2-x}\text{Sr}_x\text{CuO}_4$ and $\text{Y}_{1-x}\text{Ca}_x\text{Ba}_2\text{Cu}_3\text{O}_6$ as Seen by Muon Spin Rotation. *Phys. Rev. Lett.* **80**, 3843-3846 (1998).

66. Hasselmann, N., Castro Neto, A. H. and Morais Smith, C. Spin-glass phase of cuprates. *Phys. Rev. B* **69**, 014424 (2004).

Methods.

Thin-film synthesis.

$\text{La}_{3-x-y}\text{Pr}_x\text{Sm}_y\text{Ni}_2\text{O}_7$ thin films were deposited on SrLaAlO_4 (001) substrates (MTI Corporation) via the gigantic-oxidative atomic-layer-by-layer epitaxy (GOALL-Epitaxy) method²⁹. Two compositions were investigated in this study, which includes: (i) $\text{La}_{2.46}\text{Pr}_{0.24}\text{Sm}_{0.3}\text{Ni}_2\text{O}_7$ thin film ($x = 0.24, y = 0.3$), and (ii) $\text{La}_{2.85}\text{Pr}_{0.15}\text{Ni}_2\text{O}_7$ thin film ($x = 0.15, y = 0$). The growth parameters were identical to those reported previously⁵. After growth, the $\text{La}_{2.85}\text{Pr}_{0.15}\text{Ni}_2\text{O}_7$ film is post-annealed in an oxidation chamber equipped with an ambient-pressure ozone generator and *in-situ* resistance monitoring; whereas the $\text{La}_{2.46}\text{Pr}_{0.24}\text{Sm}_{0.3}\text{Ni}_2\text{O}_7$ film is untreated.

The X-ray diffraction (XRD) patterns (Extended Data Fig. 1a) reveal consecutive Bragg peaks along the out-of-plane axis without indication of impurity phases, confirming periodicity and crystallinity within only three unit cells. Reflection high-energy electron diffraction (RHEED) oscillations (Extended Data Fig. 1b) reveal that successive atomic layers were deposited layer by layer onto the SrLaAlO_4 (001) substrate by laser ablation of the respective targets, reflecting the stoichiometry and coverage of the film. The stable oscillation amplitude indicates highly reproducible growth kinetics for each monolayer and precise control of stoichiometry.

Standard Hall bar electrodes with Pt were deposited by magnetron sputtering with a shadow mask. The electrodes were bonded to sample holders with Al wires.

Transport measurements

The transport measurements were carried out in two commercial physical property measurement systems from Quantum Design: a Re-liquefier system with a 16 T-magnet (PPMS-16 T) and a cryogen-free system with a 14 T-magnet (PPMS Dynacool-14 T). The PPMS-16 T is equipped with a rotator with an accuracy of 0.053° , and the PPMS Dynacool-14 T is equipped with a high-resolution rotator with an accuracy of 0.011° . The $R_s(T)$, $R_s(B)$, $R_{yx}(B)$ results are measured in PPMS-16 T and PPMS Dynacool-14 T.

For the controlled measurements with d.c. current, an AC/DC current source meter

(Keithley 6221) was used to apply a d.c. current, and a nanovoltmeter (Keithley 2182 A) was used to measure the voltage. For the controlled measurements with a.c. current, an AC/DC current source meter (Keithley 6221) was used to apply an a.c. current, and a lock-in amplifiers (Stanford Research Systems SR830) were used to measure voltage.

Two cryogenic transverse InAs Hall sensors (Lakeshore HGCT-3020) were used to calibrate the values of the applied magnetic fields.

The $\text{La}_{2.46}\text{Pr}_{0.24}\text{Sm}_{0.3}\text{Ni}_2\text{O}_7$ thin film was firstly measured in PPMS-16 T. Then, the $\text{La}_{2.46}\text{Pr}_{0.24}\text{Sm}_{0.3}\text{Ni}_2\text{O}_7$ thin film was transferred to the PPMS Dynacool-14 T system for further measurements, accompanied by a Hall sensor. Also, the $\text{La}_{2.85}\text{Pr}_{0.15}\text{Ni}_2\text{O}_7$ thin film was firstly measured in the PPMS-16 T system. Then, the $\text{La}_{2.85}\text{Pr}_{0.15}\text{Ni}_2\text{O}_7$ thin film was transferred to the PPMS Dynacool-14 T system for further measurements, accompanied by the Hall sensor.

During the transfer between the two systems, the films were briefly exposed to room-temperature atmospheric environment. The T_c was slightly decreased, possibly due to the loss of oxygen²⁶ during the transfer at room temperature. Importantly, the key superconducting properties, such as the hysteresis behaviors, remain qualitatively consistent.

For the time-dependent resistance measurement, the applied magnetic field to polarize the sample is 1 T for $\text{La}_{2.46}\text{Pr}_{0.24}\text{Sm}_{0.3}\text{Ni}_2\text{O}_7$ thin film, and 5 T for $\text{La}_{2.85}\text{Pr}_{0.15}\text{Ni}_2\text{O}_7$ thin film. It should be mentioned that the time-dependent resistance variations show negligible change with different polarization magnetic fields, once it is above the saturated fields of the magnetoresistance hysteresis (Extended Data Fig. 8a). In the Fig. 5 for $\text{La}_{2.46}\text{Pr}_{0.24}\text{Sm}_{0.3}\text{Ni}_2\text{O}_7$ thin film and Extended Data Fig. 7 for $\text{La}_{2.85}\text{Pr}_{0.15}\text{Ni}_2\text{O}_7$ thin film, the magnetic fields are reduced to zero at a rate of 10 mT/s. This is the maximum rate of our system, which also gives the largest resistance variations during relaxations (Extended Data Fig. 8b).

Oxygen content control

The oxygen content control follows the previously reported methodology²⁶. In the PPMS systems under a vacuum environment (~ 10 Torr helium gas), the progressive resistance increase was observed above 200 K, which is attributed to the spontaneous oxygen loss from the films. To systematically control the oxygen content, from $p = 0.67$ to $p = 0.48$, we kept the samples at 300 K for approximately 45-minute intervals in the

PPMS. Consequently, the overall resistance values increase, and the superconducting transition is suppressed in a controllable manner.

Phenomenological formula for critical magnetic fields

To describe the temperature-dependent magnetic critical fields along in-plane and out-of-plane orientations $B_{c//}(T)$ and $B_{c\perp}(T)$, we use the phenomenological Ginzburg-Landau (G-L) formula³⁵ for 2D superconductors (based on the orbital pair-breaking effect under 2D confinement):

$$B_{c\perp}(T) = \frac{\phi_0}{2\pi\zeta_{G-L}^2(0)} \left(1 - \frac{T}{T_c}\right) \quad (1)$$

$$B_{c//}(T) = \frac{\sqrt{12}\phi_0}{2\pi\zeta_{G-L}(0)d_{sc}} \left(1 - \frac{T}{T_c}\right)^{\frac{1}{2}} \quad (2)$$

where ϕ_0 is the flux quantum, $\zeta_{G-L}(0)$ is the zero-temperature G-L coherence length, and d_{sc} is the superconducting thickness.

Exclusion of the extrinsic mechanisms for the hysteresis

First of all, it should be emphasized that all critical experimental results, including the hysteresis magnetoresistance with coincident minima and singular θ -dependence, and the resistance relaxations, are consistently reproduced in two samples: a $\text{La}_{2.46}\text{Pr}_{0.24}\text{Sm}_{0.3}\text{Ni}_2\text{O}_7$ film and a $\text{La}_{2.85}\text{Pr}_{0.15}\text{Ni}_2\text{O}_7$ film, which is highly suggestive of the intrinsic and universal nature of the TRS-broken glass-like superconducting state. Second, we rule out the issue of the remanent magnetic field in our measurement system. The observed temperature- and magnetic field orientation-dependence of the hysteresis loops cannot be attributed to the possible remanent field of the system, since the remanent field should not vary with temperatures and rotation angles of the sample. Moreover, the magnetic fields are calibrated by an InAs Hall sensor (Extended Data Fig. 2 and Supplementary Information Fig. S14). Furthermore, we measured a conventional superconductor Nb thin film in the same equipment, the $R_s(B)$ curves show no distinguishable hysteresis feature (Extended Data Fig. 9). These results unambiguously exclude the possible artifacts related to the magnet in the measurement system.

Our results cannot be explained by the extrinsic magnetism from magnetic impurities or external environments. Otherwise, the broken-TRS should manifest in both the 1st

and 2nd superconducting phase equivalently (note that all components are non-magnetic, including the SrLaAlO₄ substrates, Pt electrodes, and Al wires). The hysteresis is only observed in the 2nd superconducting phase with no detectable signature in the 1st superconducting phase (Fig. 2 and 3). Furthermore, the oxygen-dependence of the hysteresis pins down the involvement of electronic orbitals of Ni (Fig. 4), precluding the extrinsic and electronic orbitals-irrelevant possibilities such as vortices dynamics and magnetic impurities (which also includes the rare-earth elements La, Pr, Sm).

Exclusion of the trapped vortices as the possible mechanism for the hysteresis

First of all, hysteresis is observed under in-plane magnetic fields, despite the absence of field-induced vortices due to the confined dimensionality. Second, the 1st superconducting phase shows no hysteretic behavior, where the vortices and pinning sites should still exist. Third, several key features of the observed hysteresis explicitly contradict the behaviors of trapped vortices at grain boundaries in granular films (referred to as two-level critical-state model)⁵¹. From the perspective of the material systems, our films are pure-phase single-crystalline⁵, instead of the inhomogeneous granular films. From the perspective of hysteresis behaviors, our $R_s(B)$ curves under opposite swept magnetic fields exhibit coincident minima at 0 T (confirmed by the Hall sensor). This behavior is fundamentally against the trapped vortices scenario, where two sharply split minima emerge at symmetric magnetic fields, resultant from the cancellation between the trapped flux and the applied magnetic field. Additionally, the minima at 0 T remain identical regardless of the maximum applied field (Supplementary Information Fig. S7 and Fig. S11), inconsistent with the dependence that the minima shift to higher magnetic field with the increased maximum field in the trapped vortices model. Moreover, the hysteresis in the $R_s(B)$ curves remains qualitative invariant even when the measurement current changes by two orders of magnitudes (Supplementary Information Fig. S12). This current-independence indicates that the vortex dynamics is not dominant, since a larger driving current would induce a stronger Lorentz force to de-pin the vortices. Therefore, the observed hysteresis in the (La, Pr, Sm)₃Ni₂O₇ films should not be ascribed to the trapped vortices.

Singular polar angle-dependence of the magnetoresistance hysteresis behaviors

To confirm the reproducibility of the singular θ -dependent hysteric behaviors, we performed the magnetoresistance measurements in the La_{2.85}Pr_{0.15}Ni₂O₇ film in PPMS Dynacool-14 T, which yields a consistent polar angle-dependent hysteresis behavior (Extended Data Fig. 6). The hysteresis loop manifests a shrink, close, and re-open

process with θ increasing from 80° to 90° . With θ further increasing from 90° to 100° , the hysteresis loop shrinks, closes, and re-opens, reversing the behaviors from 80° to 90° . The $\Delta R_s(B)$ curves and the polar angle-dependent $\Delta R_{s, \max}(\theta)$ are derived. $\Delta R_{s, \max}(\theta)$ are defined as the maximum values of $\Delta R_s(B) = R_s^\uparrow(B) - R_s^\downarrow(B)$ at different θ , where \uparrow denotes magnetic fields from -15 T to 15 T, and \downarrow in reverse. The $\Delta R_{s, \max}(\theta)$ exhibit a very abrupt change within a narrow θ range around $\theta = 90^\circ$. With θ increasing from 80° to 90° or from 100° to 90° , the $\Delta R_{s, \max}(\theta)$ decreases rapidly from positive values, goes across zero (as indicated by the black dash line), and reaches the negative maximum around $\theta = 90^\circ$ (in-plane orientations). The $\Delta R_{s, \max}(\theta)$ manifests a symmetric dip centered at $\theta = 90^\circ$, supporting that the singular θ -dependence of hysteresis is correlated with the in-plane magnetic field.

Data availability

All data needed to evaluate the conclusions in the study are present in the paper and/or the Supplementary Information. The data that support the findings of this study are available from the corresponding author upon request.

Acknowledgements

We acknowledge the discussions with Yi-feng Yang and Ziqiao Wang. We thank Meixuan Li for the assistance. This work was financially supported by the National Natural Science Foundation of China [Grant No. 12488201 (J.W.)], the Innovation Program for Quantum Science and Technology [2021ZD0302403 (J.W.)], the National Key Research and Development Program of China [No. 2024YFA1408101 (Z.C.), No. 2022YFA1403101 (Z.C.), No. 2023YFA1406500 (Y.L.), No. 2022YFA1403103 (Y.L.)], the Natural Science Foundation of China [Grant No. 92265112 (Z.C.), Grant No. 12374455 (Z.C.), Grant No. 52388201 (Z.C.), Grant No. 12174442 (Y.L.)], Young Elite Scientists Sponsorship Program by CAST [No. 2023QNRC001 (Y.L.)], Young Elite Scientists Sponsorship Program by BAST [No. BYESS2023452 (Y.L.)], the Fundamental Research Funds for the Central Universities and the Research Funds of Renmin University of China [No. 22XNKJ20 (Y.L.)], the Guangdong Provincial Quantum Science Strategic Initiative [Grant No. GDZX2401004 (Z.C.), Grant No. GDZX2201001 (Z.C.)], the Shenzhen Science and Technology Program [Grant No. KQTD20240729 102026004 (Z.C.)], and the Shenzhen Municipal Funding Co-construction Program Project [Grant No. SZZX2301004 (Z.C.), Grant No. SZZX2401001 (Z.C.)], the China Postdoctoral Science Foundation [Grant No. 2024M760063 (H.R.J)], Z.W. is supported by the U.S. Department of Energy, Basic

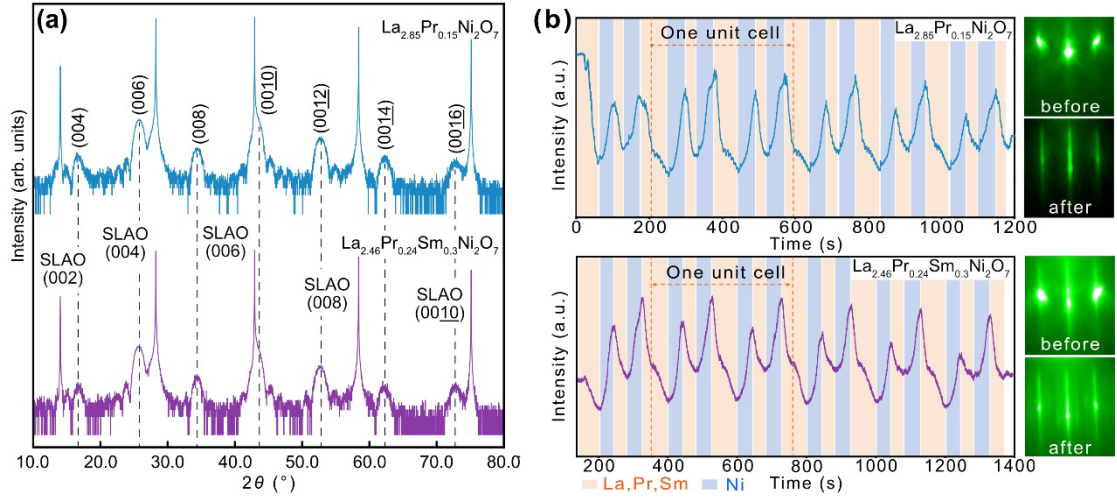
Energy Sciences Grant DE-FG02-99ER45747, G.-M.Z. acknowledges the support from the National Key Research and Development Program of MOST of China [Grant No. 2023YFA1406400], H. W. acknowledges the support from the China Postdoctoral Science Foundation [Grant No. GZB20240294 and Grant No. 2024M751287]. Z. C. acknowledges the support from International Station of Quantum Materials.

Author contributions

J.W. conceived the project. J. W. and Z.C. supervised the project. H.J., Z.X. and L.P. performed the transport measurements and analyzed the data under the guidance of J.W.. Y.C., G.Z., H.W. and H.H. performed the thin-film growth under the guidance of Q.-K.X. and Z.C. J.G. and Y.L. provided the support in data interpretation. G.-M.Z. and Z.W. contributed to the theoretical explanations. H.J., Y.L., Z.W. and J.W. wrote the manuscript with input from all other authors. H.J., Z.X., Y.C. and G.Z. contributed equally to this work.

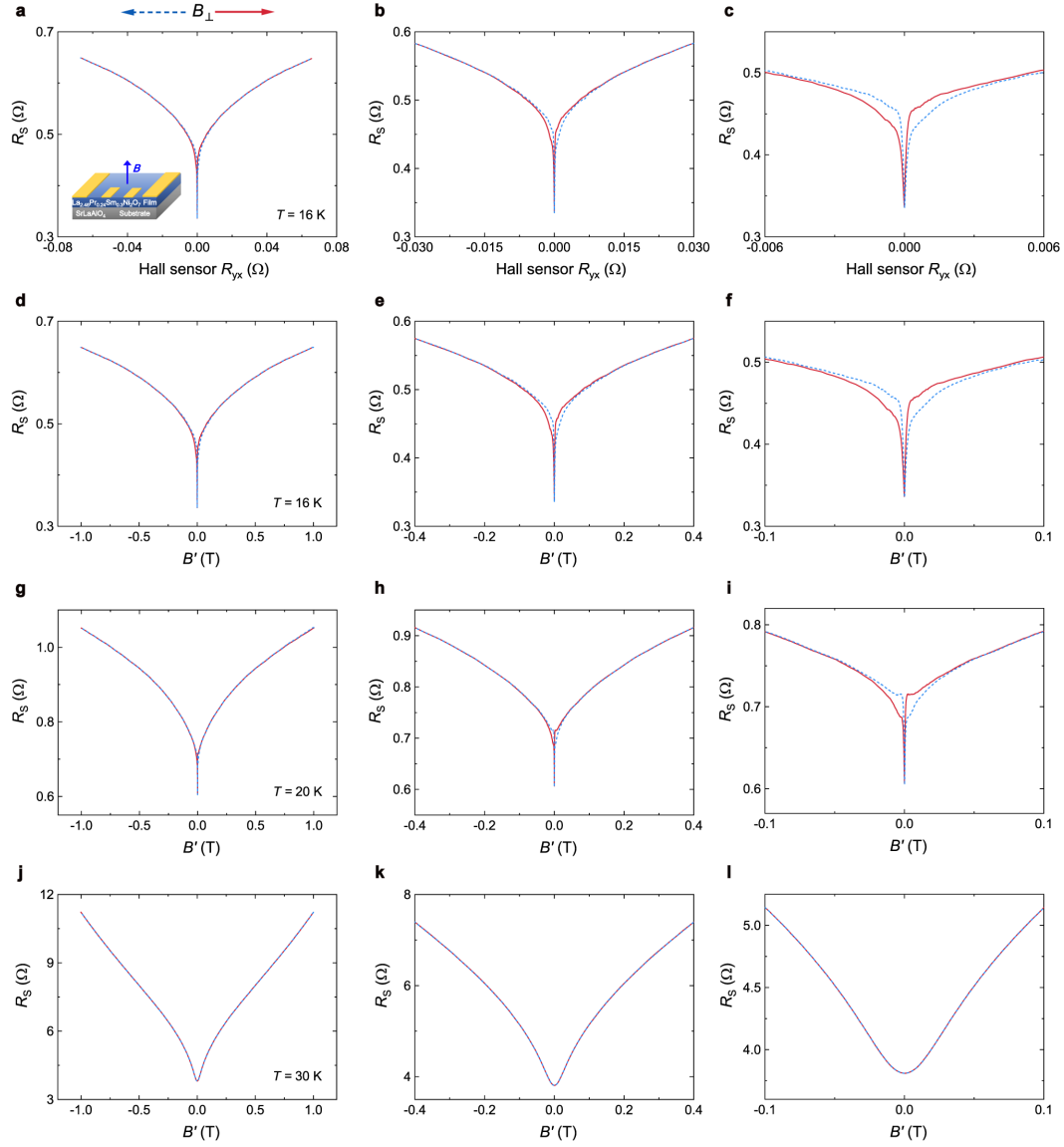
Competing interests

The authors declare no competing interests.

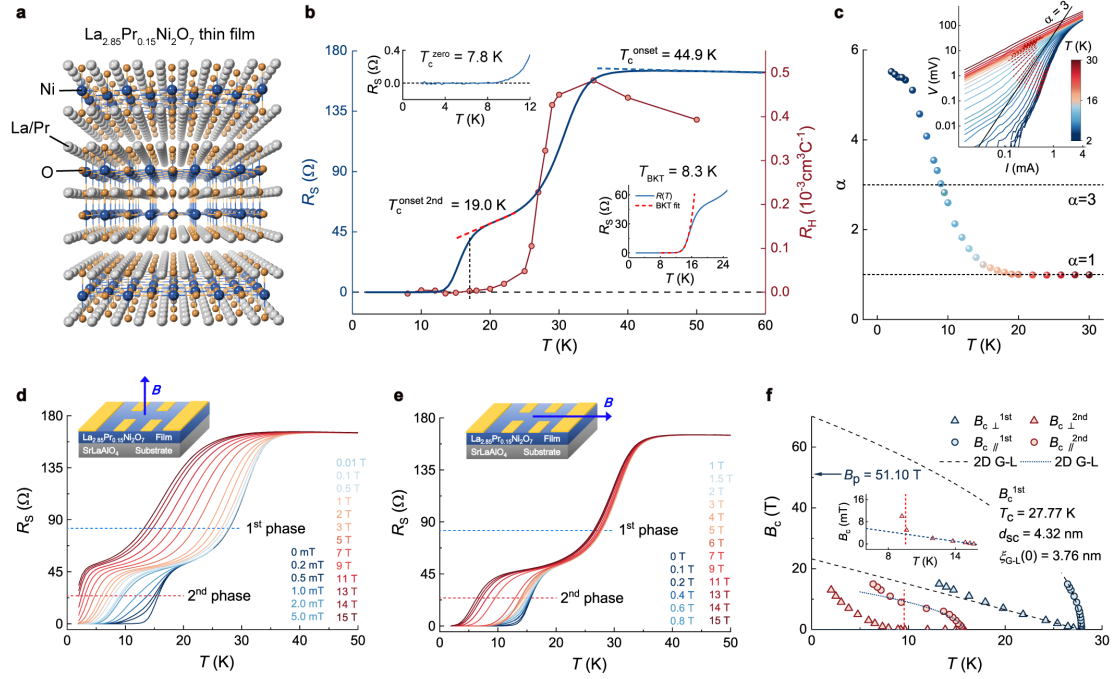


Extended Data Fig. 1 | XRD and RHEED oscillations of bilayer nickelate thin films.

a, X-ray diffraction (XRD) along the out-of-plane axis of a 3UC $\text{La}_{2.85}\text{Pr}_{0.15}\text{Ni}_2\text{O}_7$ film and a 3UC $\text{La}_{2.46}\text{Pr}_{0.24}\text{Sm}_{0.3}\text{Ni}_2\text{O}_7$ film growth on SrLaAlO_4 substrate. **b**, Reflection high-energy electron diffraction (RHEED) oscillation and patterns of the above-mentioned film. Blue and orange block represent the growth of $(\text{La}_{0.95}\text{Pr}_{0.05})\text{O}_x/(\text{La}_{0.82}\text{Pr}_{0.08}\text{Sm}_{0.1})\text{O}_x$ and NiO_x layer, respectively.

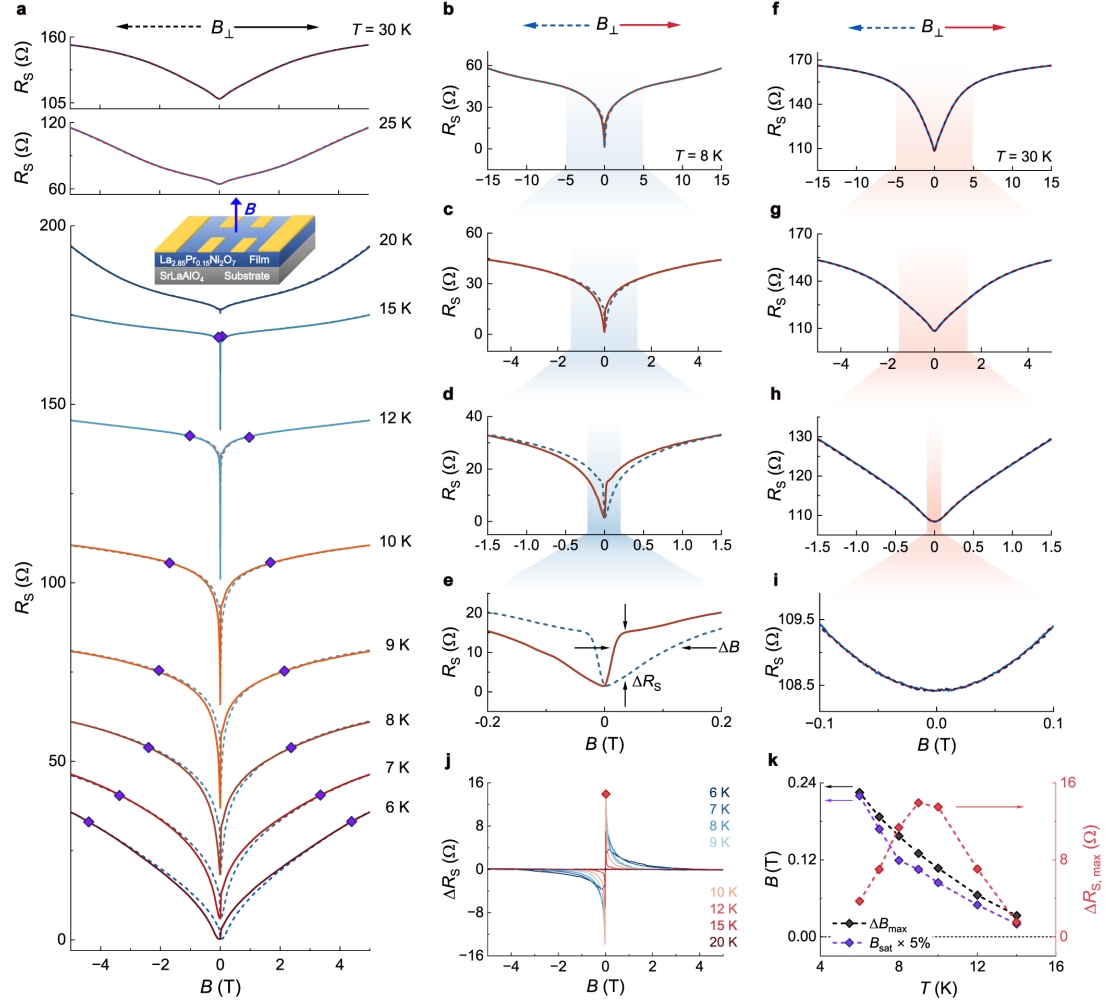


Extended Data Fig. 2 | Magnetoresistance of $\text{La}_{2.46}\text{Pr}_{0.24}\text{Sm}_{0.3}\text{Ni}_2\text{O}_7$ film with the magnetic field values calibrated by a Hall sensor (Lakeshore HGCT-3020). **a to c,** Sheet resistance R_s of the $\text{La}_{2.46}\text{Pr}_{0.24}\text{Sm}_{0.3}\text{Ni}_2\text{O}_7$ thin film as a functional of the Hall resistance R_{yx} of the Hall sensor at 16 K, under the opposite swept out-of-plane magnetic fields. **d to f,** R_s of the $\text{La}_{2.46}\text{Pr}_{0.24}\text{Sm}_{0.3}\text{Ni}_2\text{O}_7$ thin film as a functional of the calibrated magnetic fields B' at 16 K, showing the evident hysteresis with coincident minima at 0 T. The B' is derived from the R_{yx} of the Hall sensor, by B' (in Tesla) = 14.97 R_{yx} (in Ohm). **g to i,** R_s as a function of B' at 20 K (**g to i,**) and 30 K (**j to l,**) where the hysteresis persists at 20 K and is indiscernible at 30 K. The measurement was performed in the PPMS Dynacool-14 T system. Complementary data can be found in Supplementary Information Fig. S5 and Fig. S6.



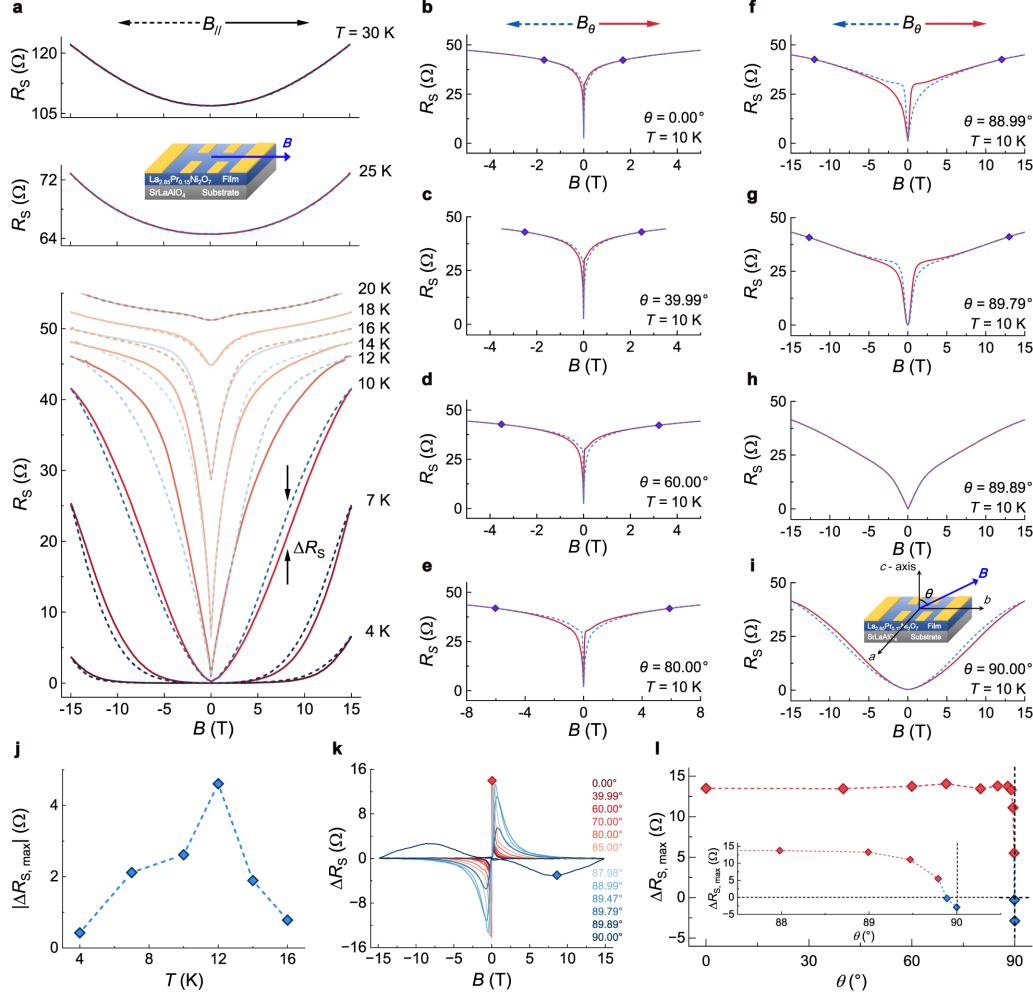
Extended Data Fig. 3 | Superconductivity in bilayer nickelate $\text{La}_{2.85}\text{Pr}_{0.15}\text{Ni}_2\text{O}_7$ thin film. **a**, Crystal structure of the $\text{La}_{2.85}\text{Pr}_{0.15}\text{Ni}_2\text{O}_7$ film. **b**, Temperature-dependent sheet resistance $R_s(T)$ curve (left axis) and Hall coefficient $R_H(T)$ curve (right axis). $R_H(T)$ drops to zero around 17 K, as indicated by the vertical black dash line. $T_c^{\text{onset}} = 44.9$ K and $T_c^{\text{onset 2nd}} = 19.0$ K are defined by deviation from the extrapolation of the normal state (blue dash line) and the $R_s(T)$ step around 20 K (red dash line), respectively. Upper inset shows the enlarged view of $R_s(T)$ curve around $T_c^{\text{zero}} = 7.8$ K, below which the sheet resistance reaches zero within the noise level of the measurement system. Lower inset shows the $R_s(T)$ curve and the fit curve for Berezinskii-Kosterlitz-Thouless (BKT) transition, yielding a BKT temperature $T_{\text{BKT}} = 8.3$ K. **c**, Temperature-dependent α determined by $V \sim I^\alpha$. With increasing temperatures, α drops to 3 at $T_{\text{BKT}} = 8.9$ K. Inset: V - I curves from 2 K to 30 K. Red dash lines correspond to the power-law dependence $V \sim I^\alpha$. Black solid line denote $V \sim I^\alpha$ where $\alpha = 3$. **d**, **e** $R_s(T)$ curves under out-of-plane magnetic fields (B_\perp , **d**), and in-plane magnetic fields (B_\parallel , **e**). Insets show the measurement configurations with Hall bar geometry. Blue and red dash lines correspond to 50% R_N - and 50% $R_s^{\text{onset 2nd}}$ -criteria used to determine the critical magnetic field B_c for the 1st (blue) and 2nd (red) superconducting phases, respectively. **f**, Temperature-dependent $B_c(T)$ for the 1st (blue symbols) and 2nd (red symbols) superconducting phases along out-of-plane (triangles) and in-plane (circles) directions. Dash and dot lines are the 2D Ginzburg-Landau (G-L) fittings of the $B_c(T)$ near T_c . Blue arrow marks the Pauli limit, $B_p = 51.10$ T, estimated by B_p (in Tesla) = $1.84T_c$ (in Kelvin). Inset shows the zoomed-in view of $B_{c\perp}^{\text{2nd}}$. The measurement was performed

in the PPMS-16 T system.



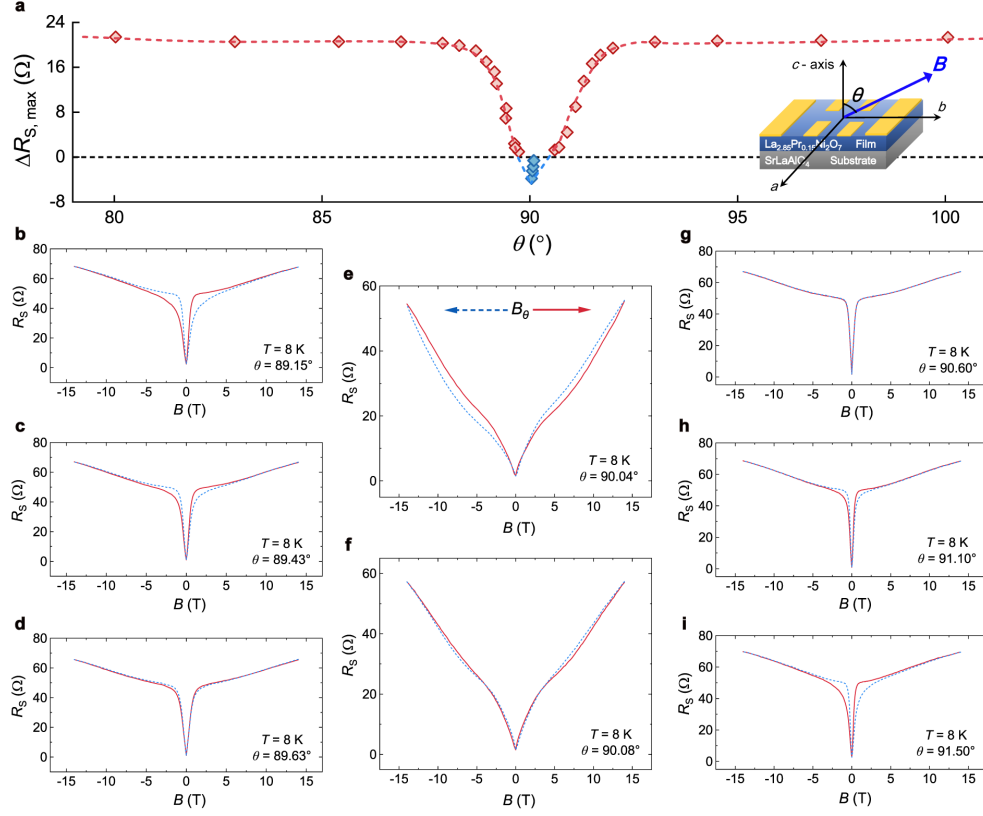
Extended Data Fig. 4 | Hysteretic magnetoresistance in $\text{La}_{2.85}\text{Pr}_{0.15}\text{Ni}_2\text{O}_7$ thin film under out-of-plane magnetic fields. **a**, $R_s(B)$ curves at different temperatures, zoomed-in to $|B_\perp| \leq 5$ T. Curves are offset vertically for clarity. Here, all $R_s(B)$ curves are measured with B_\perp sweeping from 15 T to -15 T (dash lines) and -15 T to 15 T (solid lines), while the selected ranges of $R_s(B)$ curves are displayed for clarity. The hysteresis is observed below 15 K and disappears at higher temperatures. Purple diamonds indicate the saturation fields B_{sat} . Inset shows the measurement configuration. **b-e**, Representative $R_s(B)$ curves from **a** at $T = 8$ K with B_\perp ranging within 15 T (**b**), 5 T (**c**), 1.5 T (**d**), 0.2 T (**e**), which show the prominent hysteretic loop. **f-i**, Representative $R_s(B)$ curves at $T = 30$ K within 15 T (**f**), 5 T (**g**), 1.5 T (**h**), 0.1 T (**i**), where no hysteresis loop could be distinguished. The shadows denote the zoomed-in ranges. **j**, $\Delta R_s(B)$ curves, derived by $R_s^\uparrow(B) - R_s^\downarrow(B)$. One representative $\Delta R_s(B)$ peak to determine $\Delta R_{s,\text{max}}$ (red diamond) is marked. **k**, Temperature-dependent ΔB_{max} , $B_{\text{sat}} \times 5\%$ (left axis),

and $\Delta R_{S, \max}$ (right axis). The measurement was performed in the PPMS-16 T system. The magnetoresistance hysteresis with the magnetic field values calibrated by a Hall sensor can be found in Supplementary Information Fig. S14 and Fig. S15.

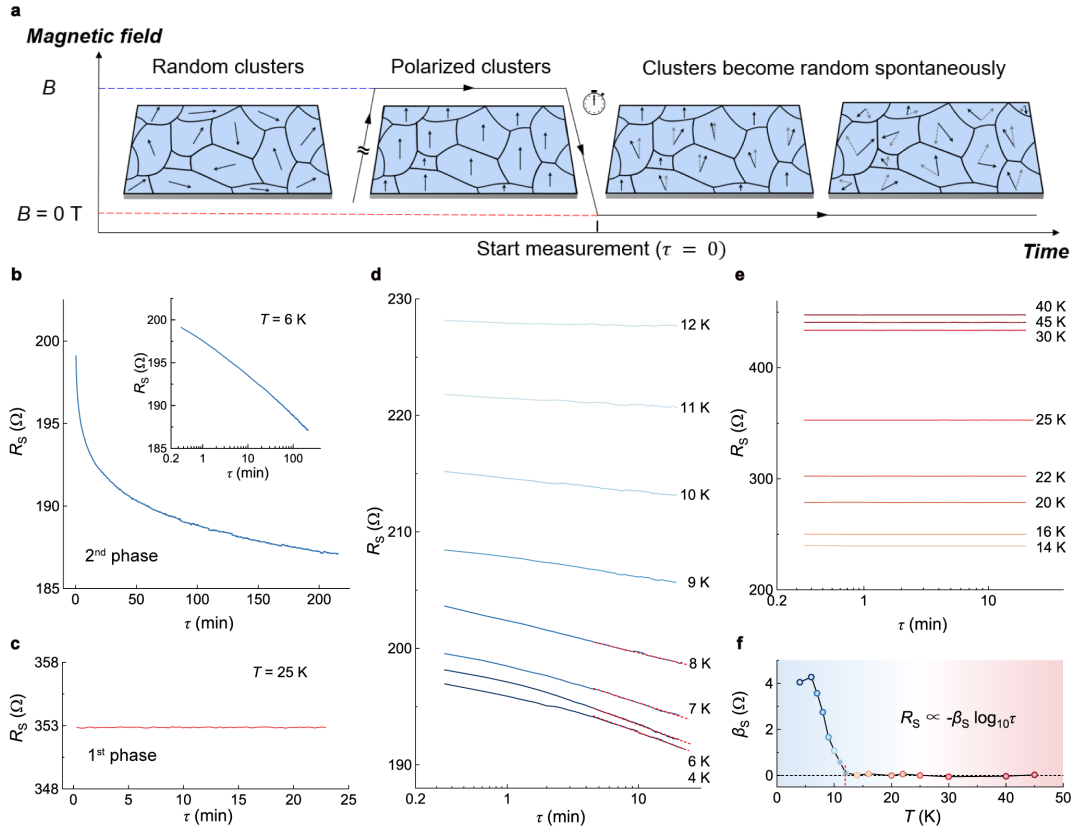


Extended Data Fig. 5 | Hysteretic magnetoresistance in $\text{La}_{2.85}\text{Pr}_{0.15}\text{Ni}_2\text{O}_7$ thin film under magnetic fields along different orientations. **a**, $R_S(B)$ curves at different temperatures with B_{\parallel} sweeping from 15 T to -15 T (dash lines) and -15 T to 15 T (solid lines). The hysteresis is observed below 18 K and disappears at higher temperatures. Inset shows the measurement configuration. **b-i**, Representative $R_S(B)$ curves at $T = 10$ K with the opposite swept magnetic fields B_{θ} along different polar angles θ from 0° (out-of-plane) to 90° (in-plane), as denoted in the figures. Purple diamonds denote the saturation fields. **j**, Temperature-dependent $|\Delta R_{S, \max}|$ under in-plane magnetic fields. **k**, Anti symmetrized $\Delta R_S(B)$ curves at different θ angles, where the $\Delta R_{S, \max}$ at $\theta = 0^\circ$ (defined as positive polarity, red diamond) and 90° (defined as negative polarity, blue

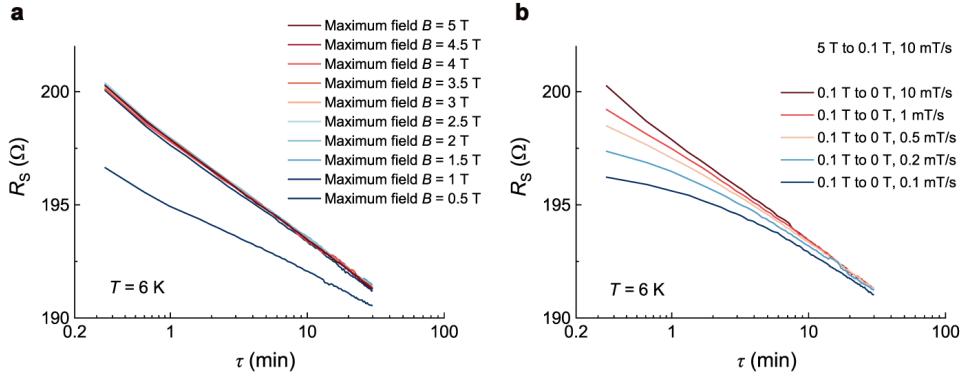
diamond) are marked. **1**, θ -dependence of $\Delta R_{S, \max}$. Red and blue colors highlight the positive and negative polarities. Inset shows the zoomed-in view around $\theta = 90^\circ$ (in-plane). Black dash lines are guides to the eye. The measurement was performed in the PPMS-16 T system.



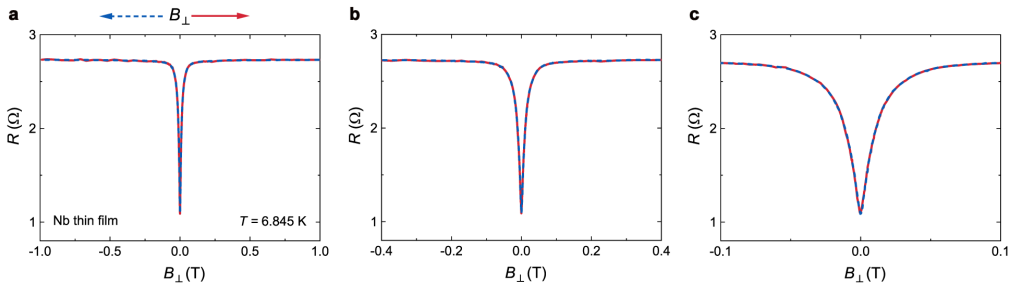
Extended Data Fig. 6 | Polar angle θ -dependence of hysteresis in $\text{La}_{2.85}\text{Pr}_{0.15}\text{Ni}_2\text{O}_7$ film measured in PPMS Dynacool-14 T system. **a, Polar angle θ -dependence of the maxima resistance difference of the hysteresis $\Delta R_{S, \max}$, which is symmetric with respect to $\theta = 90^\circ$ (in-plane). The dash line is a guide to the eye. **b** to **i**, Magnetoresistance $R_S(B_\theta)$ at $T = 8$ K with B_θ along different θ . The measurement was performed in the PPMS Dynacool-14 T system.**



Extended Data Fig. 7 | Time-dependent resistance relaxations in the $\text{La}_{2.85}\text{Pr}_{0.15}\text{Ni}_2\text{O}_7$ thin film with $p = 0.48$. **a**, Schematic illustration of the measurement process. At a fixed temperature, an external magnetic field, exceeding the saturated field of the hysteresis, is applied to fully polarize the random glass clusters. Then, the external magnetic field is reduced to zero. Upon reaching zero field, the time-dependent resistance measurements initiate at the counting time $\tau = 0$. **b**, Time-dependent sheet resistance $R_s(\tau)$ at 6 K, exhibit a gradual decrease over time. Inset shows $R_s(\tau)$ from **b** on a logarithmic time-scale. **c**, $R_s(\tau)$ at 25 K, which remains invariant over time within the resolution. **d**, $R_s(\tau)$ below 12 K, showing nearly logarithmic time-dependence. **e**, $R_s(\tau)$ above 14 K, showing no discernable time-dependent variation. **f**, Temperature-dependence of the exponent β , extracted from $R_s \propto -\beta \log_{10} \tau$. Red dash lines in **d** are the fit curves to extract β . The measurement was performed in the PPMS Dynacool-14 T system.



Extended Data Fig. 8 | Time-dependent resistance relaxations in the $\text{La}_{2.85}\text{Pr}_{0.15}\text{Ni}_2\text{O}_7$ film with $p = 0.48$, measured under different conditions. a, $R_s(\tau)$ curves measured with different magnetic fields for the polarization. The $R_s(\tau)$ curves overlaps when the applied polarization fields are larger than 1 T, approximately the hysteresis saturated fields for $p = 0.48$. The $R_s(\tau)$ values are significantly diminished when the applied polarization field is merely 0.5 T, smaller than the saturated fields. b, $R_s(\tau)$ curves measured with different rates, at which the polarization magnetic fields are reduced to zero. From 5 T to 0.1 T, the rates are all 10 mT/s. From 0.1 T to 0 T, the rates are changed, as denoted in the figures. The $R_s(\tau)$ variations are stronger with faster removal of magnetic fields to zero. The measurement was performed in the PPMS Dynacool-14 T system.



Extended Data Fig. 9 | Absence of hysteresis in a 30-nm thick Nb thin film. a to c, Magnetoresistance $R_s(B)$ curves under opposite swept magnetic fields at 6.845 K in a 30-nm thick Nb thin film with different zoomed-in scales, where no hysteresis loop is observed. The Nb thin film and the electrodes with Hall bar geometry are fabricated using the standard photolithography technique. The Nb thin film is grown by magnetron sputtering. The electrodes are grown by electron beam evaporation. The measurement was performed in the PPMS-16 T system, the same instrument as the $\text{La}_{2.46}\text{Pr}_{0.24}\text{Sm}_{0.3}\text{Ni}_2\text{O}_7$ and $\text{La}_{2.85}\text{Pr}_{0.15}\text{Ni}_2\text{O}_7$ thin film.